

Discovery of Novel Potent VEGFR-2 Inhibitors Exerting Significant Antiproliferative Activity against Cancer Cell Lines

Yanmin Zhang, Yadong Chen, Danfeng Zhang, Lu Wang, Tao Lu, and Yu Jiao

J. Med. Chem., **Just Accepted Manuscript** • DOI: 10.1021/acs.jmedchem.7b01091 • Publication Date (Web): 30 Nov 2017

Downloaded from <http://pubs.acs.org> on November 30, 2017

Just Accepted

“Just Accepted” manuscripts have been peer-reviewed and accepted for publication. They are posted online prior to technical editing, formatting for publication and author proofing. The American Chemical Society provides “Just Accepted” as a free service to the research community to expedite the dissemination of scientific material as soon as possible after acceptance. “Just Accepted” manuscripts appear in full in PDF format accompanied by an HTML abstract. “Just Accepted” manuscripts have been fully peer reviewed, but should not be considered the official version of record. They are accessible to all readers and citable by the Digital Object Identifier (DOI®). “Just Accepted” is an optional service offered to authors. Therefore, the “Just Accepted” Web site may not include all articles that will be published in the journal. After a manuscript is technically edited and formatted, it will be removed from the “Just Accepted” Web site and published as an ASAP article. Note that technical editing may introduce minor changes to the manuscript text and/or graphics which could affect content, and all legal disclaimers and ethical guidelines that apply to the journal pertain. ACS cannot be held responsible for errors or consequences arising from the use of information contained in these “Just Accepted” manuscripts.

Discovery of Novel Potent VEGFR-2 Inhibitors Exerting Significant Antiproliferative Activity against Cancer Cell Lines

Yanmin Zhang^a, Yadong Chen^a, Danfeng Zhang^b, Lu Wang^b, Tao Lu^{a,b,c}, Yu Jiao^{b*}*

^a Laboratory of Molecular Design and Drug Discovery, School of Science, China Pharmaceutical University, 639 Longmian Avenue, Nanjing 211198, China.

^b School of Science, China Pharmaceutical University, 639 Longmian Avenue, Nanjing 211198, China.

^c State Key Laboratory of Natural Medicines, China Pharmaceutical University, 24 Tongjixiang, Nanjing 210009, China.

ABSTRACT Computational and experimental studies were applied to the discovery of a series of novel vascular endothelial growth factor receptor 2 (VEGFR-2) inhibitors. Eight compounds exhibited nanomolar IC₅₀ values against VEGFR-2 and compounds **6**, **19**, **22** and **23** showed potent antiproliferative effects against several cell lines. Particularly, compound **23** behaved better than FDA approved drugs, sorafenib and sunitinib, in antiproliferative activity against cell lines related to all nine tumor types tested (GI₅₀ values), and it was better or comparable in safety (LC₅₀ values). Compound **23** even demonstrated high potency on one of the drug-resistant cell lines (NCI/ADR-RES) responsible for ovarian cancer and cell lines contributing to prostate cancer, regarded as one of the VEGF/VEGFR pathway drug-resistant tumors. This compound is

1
2
3 likely a promising candidate for the treatment of leukemia, non-small cell lung cancer (NSCLC),
4 colon cancer, ovarian cancer and breast cancer with a suitable balance of both efficacy and safety.
5
6
7

8 **INTRODUCTION**

9
10 Angiogenesis, the formation of new blood vessels by sprouting or splitting from pre-existing
11 vessels for cell proliferation, migration, and survival¹, plays a pivotal role in both normal
12 embryonic and adult development²⁻⁴. However, angiogenic abnormalities are observed in
13 numerous pathological conditions such as cancer, psoriasis, rheumatoid arthritis, inflammation,
14 and retinal complications.⁵ The specific inhibition of signal transduction via the system
15 containing vascular endothelial growth factor (VEGF) and its receptor (VEGFR) is a promising
16 approach to starve tumor cells of nutrients and thus impede tumor growth⁶ and metastasis^{7, 8}. The
17 VEGFR family, VEGFR-1 (Flt-1), VEGFR-2 [Flk-1/kinase domain receptor (KDR)] and
18 VEGFR-3 (Flt-4), which are cell surface tyrosine kinase receptors, are located on the host
19 vascular endothelium, lymphatic, and hematopoietic systems, and these family members are
20 major proteins modulating angiogenesis by transducing VEGF-A, VEGF-B, VEGF-C, VEGF-D,
21 and placental growth factor (PlGF) signals to downstream pathways^{9, 10}. Specifically, VEGFR-2
22 is regarded as one of the central targets for discovering inhibitors against tumor-associated
23 angiogenesis, as it is responsible for the transduction of the main pro-angiogenic signal for
24 vasculature.¹¹ Because most current VEGFR-2 therapeutics are ATP competitive inhibitors, they
25 exert their effect by occupying the highly conserved ATP pocket.¹² Moreover, small-molecule
26 kinase inhibitors have recently seen burgeoning growth with 28 drugs gaining approval by the
27 US Food and Drug Administration (FDA) for the treatment of cancers, such as advanced renal
28 cell carcinoma and hepatocellular carcinoma.¹³ Among these drugs, nine (sorafenib, sunitinib,
29
30
31
32
33
34
35
36
37
38
39
40
41
42
43
44
45
46
47
48
49
50
51
52
53
54
55
56
57
58
59
60

1
2
3 pazopanib, vandetanib, axitinib, regorafenib, cabozantinib, nintedanib, lenvatinib and apatinib)
4
5 involve VEGFR-2 inhibition, demonstrating the clinical benefits of VEGFR-2 inhibitors.^{13, 14}
6

7
8 However, both intrinsic and acquired resistance are major contributors to transient clinical
9
10 benefits and failure of antiangiogenic drugs in the clinic.^{15, 16} Several mechanisms have been
11
12 proposed for the drug resistance to VEGF blockade seen in some cancer patients and these
13
14 mechanisms are not mutually exclusive. For example, (1) in established tumors, the inhibition of
15
16 VEGF can aggravate hypoxia, resulting in upregulation of the production of other angiogenic
17
18 factors or increase in tumor cell invasiveness. (2) Tumor cells with other acquired mutations can
19
20 also become hypoxia tolerant. (3) Tumor vessels covered by pericytes are generally less sensitive
21
22 to VEGF inhibition. (4) Tumor vascularization begins to include intussusception, vasculogenic
23
24 mimicry and vessel growth, differentiation of putative cancer stem cells into endothelial cells,
25
26 and existing vessel co-option, etc. These changes can be rescued by recruited macrophages,
27
28 proangiogenic bone-marrow-derived cells, or activated cancer-associated fibroblasts through
29
30 producing proangiogenic factors. Regarding safety, VEGFR inhibitors all share mechanism-
31
32 related toxicities, of which the most common are hypertension, proteinuria, thromboembolism,
33
34 hemorrhage, fistula formation, bowel perforation, and reversible posterior
35
36 leukoencephalopathy.¹⁶
37
38
39
40
41

42
43 Generally, resistance to numerous other drugs by targeting specific genetic mutations often
44
45 leads to a stable, heritable, acquired drug-resistant phenotype. In contrast, to combat acquiring
46
47 resistance to antiangiogenic VEGF pathway-targeting drugs, one interesting consideration is that
48
49 the evasive/acquired resistance is potentially reversible (epigenetic), not necessarily stable, and
50
51 hence presumably immutable with host endothelial cells lining new tumor blood vessels.^{16, 17}
52
53
54 This may help explain why some anti-VEGF therapies can be administered for long periods as
55
56
57
58
59
60

1
2
3 maintenance therapy even beyond disease progression.^{18, 19} For example, therapeutic benefit is
4 observed when switching VEGFR tyrosine kinase inhibitors (TKIs) to second-line alternate
5 antiangiogenic drugs in patients with renal cell carcinoma²⁰. Regarding potential reversible
6 resistance, initial TKIs might still be effective and should be considered in future clinical trials
7 assessing subsequent-line therapies. Thus, discovery of novel VEGFR-2 inhibitors with
8 satisfactory properties that can surmount drug resistance and decrease toxicity remain a
9 substantial challenge.^{21, 22}

19 In this work, computational and experimental studies were applied to the discovery of a series
20 of novel VEGFR-2 inhibitors (**Figure 1**). First, BREED²³, a ligand hybridization methodology
21 belonging to fragment-based drug design (FBDD), was conducted on the ligands from x-ray
22 crystallographic structures of VEGFR-2, selected hit fragments from previous work²³ and the
23 KLIFS database²⁴. Then, molecular docking was used to screen the generated database. Based on
24 of the abundance of crystal structure data available, a robust linear model for the relationship
25 between predicted binding free energy (Delta G, ΔG) calculated by Molecular
26 Mechanics/Poisson–Boltzmann Surface Area (MM/PBSA) and enzyme inhibitory activity (such
27 as IC₅₀ values) was constructed after a 20 ns molecular dynamics (MD) simulation. Then,
28 potential compounds selected by molecular docking were submitted for MD simulation and
29 scored by the linear model. Ten compounds were ultimately chosen for synthesis and biological
30 activity evaluation. Those that exhibited favorable enzymatic activity and antiproliferative
31 effects on human umbilical vein endothelial cells (HUVECs) and melanoma cell line MDA-MB-
32 435 were submitted to the National Cancer Institute (NCI)-60 platform. The NCI testing
33 measured the growth percent in 58 cell lines from nine different tumor types, one of which is
34
35
36
37
38
39
40
41
42
43
44
45
46
47
48
49
50
51
52
53
54
55
56
57
58
59
60

antiangiogenic drug-resistant prostate cancer. Finally, the kinase activity profile of the most effective compound was investigated.

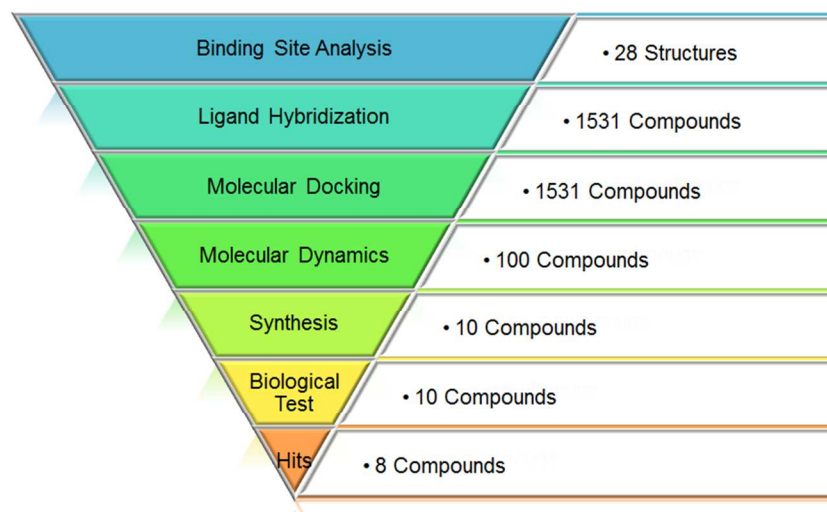


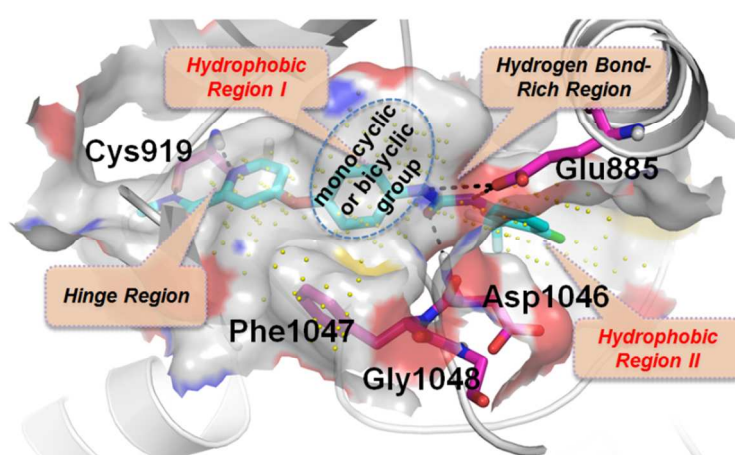
Figure 1 The workflow of for this investigation.

RESULTS AND DISSCUSSION

Binding Site Analysis and SAR Summarization

Previously, we constructed a three-dimensional quantitative structure activity relationship (3D-QSAR) model and summarized a SAR map for VEGFR-2.²⁵ Combined with molecular docking and sitemap analysis²⁶, the binding site of VEGFR-2 can be divided into four important regions (**Figure 2**). Sorafenib, for example, binds to the active site cavity of VEGFR-2 in a DFG-out (inactive) conformation, which enables the appropriately substituted inhibitor to penetrate into the extended hydrophobic pocket. The N-methyl picolinamide/N-methyl-2-pyridinecarboxamide part binds to the Hinge Region by forming two hydrogen bonds with the backbone amide NH and carbonyl oxygen of Cys919, which are the predominant forces that maintain inhibitor activity. The Hydrogen Bond-Rich Region indicates where hydrogen acceptors or donors are favorable. An effective inhibitor (here the amide group of sorafenib) will form two to three hydrogen bonds with the side chain of Glu885 and the backbone NH of Asp1046, two residues

1
2
3 that have also been implicated as important contributors to both hydrogen bonding and
4 nonbonding interactions for inhibitor binding by FTMap analysis^{27, 28}. However, we focused
5 instead on the two important hydrophobic regions. Hydrophobic Region I, occupied by the
6 central phenyl ring in sorafenib, is surrounded by several hydrophobic amino acids, including
7 Ala866, Leu840, Gly841 and Ile915. As shown in **Figure 2**, this region, probed by SiteMap
8 (yellow dots), can accommodate monocyclic or bicyclic ring structures, which may provide
9 space for additional modification. Hydrophobic Region II, is occupied by the 4-chloro-3-
10 (trifluoromethyl)benzene moiety and is surrounded by Ile892, Ile888, Leu889 and Val898. This
11 region extends to Hydrophobic Region II and bypasses the DFG moiety, which is generally a
12 determinant of inhibitor selectivity.
13
14
15
16
17
18
19
20
21
22
23
24
25



26
27
28
29
30
31
32
33
34
35
36
37
38
39
40
41
42 **Figure 2** The binding site of VEGFR-2 in complex with sorafenib (PDB ID: 3EWH).
43
44

45 **BREED**

46
47 Herein, in addition to the 28 crystal structures of VEGFR-2¹⁴, selected hit fragments from
48 previous work²³ and 1100 human kinase-ligand cocrystal complexes of various targets from the
49 KLIFS database (<http://www.vu-compmedchem.nl>)^{24, 29} were aligned. Because most kinases
50 possess similar binding sites, approaching this dilemma by combining the available data may
51
52
53
54
55
56
57
58
59
60

expand the possibility of chemical space for novel inhibitor scaffolds. **Figure 3a** illustrates one example, where the two known VEGFR-2 inhibitors, vandetanib (IC_{50} : 40 nM) and sorafenib (IC_{50} : 90 nM), (activity data from <http://www.selleckchem.com/>) and a hit fragment, Hit_Scaffold_4 (Bayesian Score: 35.6), from our previous study²⁹ were overlapped and swapped to generate hybridized compound **6**, which was synthesized and had 15.3 nM enzymatic activity against VEGFR-2. As shown in **Figure 3b**, the fragments of compound **6** adopt conformations remarkably similar to the original fragments extracted from crystal structures with the two known inhibitors and the hit fragment when the BREED-generated model was overlaid within the active site of the protein. The root-mean-square deviation (RMSD) values for the 6,7-dimethoxyquinazoline group, the naphthylamine portion and the 1-(4-chloro-3-(trifluoromethyl)phenyl)-3-methylurea moiety were 0.046, 0.037, and 0.054 Å, respectively, sufficiently demonstrating the reliability of the BREED method. A total of 1531 novel compounds were obtained after duplicate removal and all were submitted for further molecular docking analysis ([Docking_results_for_in-house_compound-database.zip](#) in the Supporting Information).

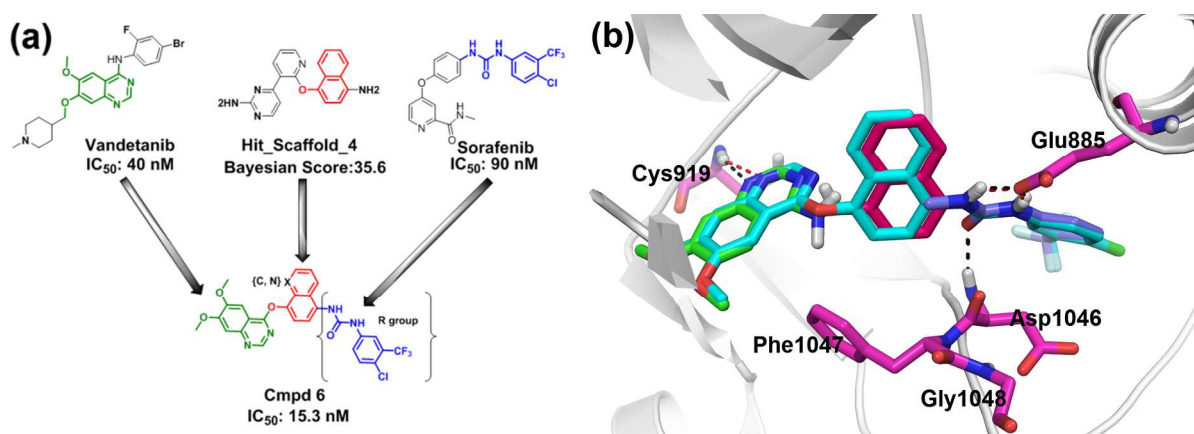
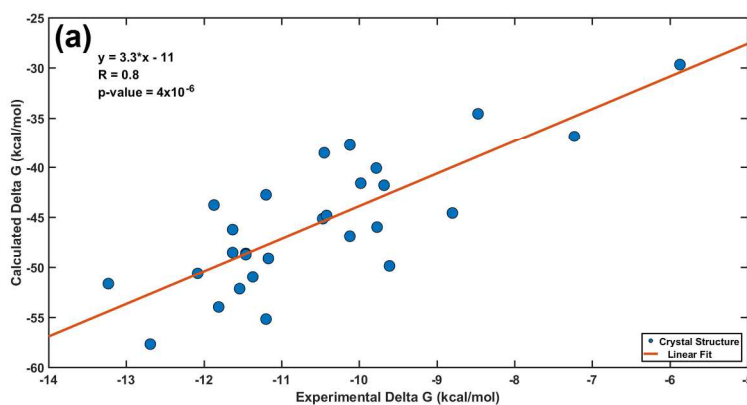


Figure 3 (a) The combinatorial approach of BREED. (b) Different colors were used to denote the scaffolds from different input structures: the 6,7-dimethoxyquinazoline group from

vandetanib (green), the naphthamide portion of Hit_Scaffold_4 (dark pink) and the 1-(4-chloro-3-(trifluoromethyl)phenyl)-3-methylurea moiety (blue). Compound **6** (Cmpd **6**) is colored cyan and important active site residues are labeled and colored magenta.

MD Linear Model and Binding Affinity Prediction

A set of 28 crystallographic structures (**Table S1**) from the Protein Data Bank (PDB)³⁰ database were used to construct the binding affinity prediction model. Of the crystallized ligands, 24 have low nanomolar (nM) IC₅₀ values (less than 100 nM) (**Table S1**) and they contain different structural scaffolds that sample diverse chemical space. For each protein, a 20 ns MD simulation was performed to ensure that dynamic equilibrium was attained (**Figure 5**). Snapshots were extracted from the last 5 ns at every 10 ps interval. A total of 500 snapshots were obtained and each was used to calculate a binding free energy, then an average of these 500 values was used. Next, the average binding free energy was converted to binding affinity (we used IC₅₀ values instead) by the following formula: $IC_{50} = \exp[\Delta G/(RT)]$, where RT is approximately 0.59 kcal/mol. A linear model was built between the computational and experimental binding free energies with a Pearson correlation coefficient (R) of 0.8 and a p-value of about 4×10^{-6} (**Figure 4a**), suggesting robustness of the model.



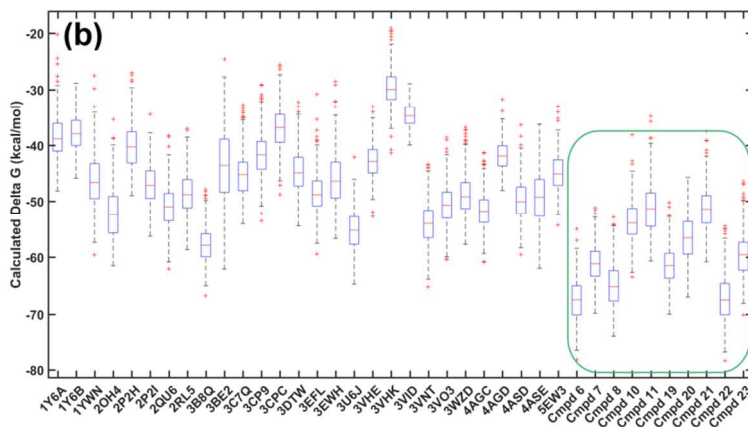
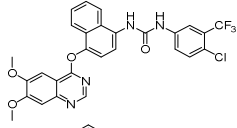
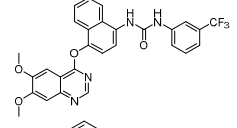
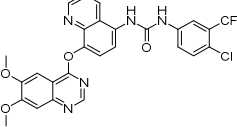
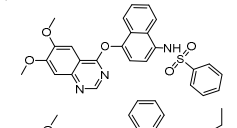
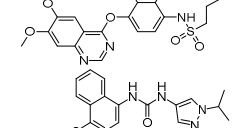
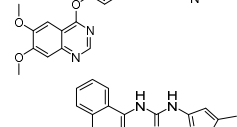
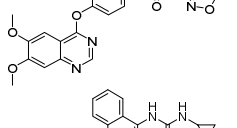
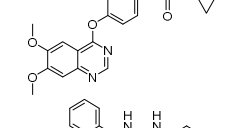
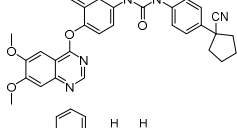
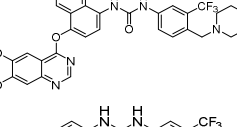
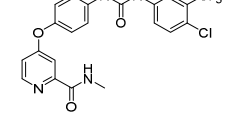


Figure 4 The binding affinity prediction model (a) and the average binding affinity of both ligands from the crystal structures and the selected compounds (b) Delta G means ΔG .

As shown in **Figure 4a**, this model ($y = 3.3 \cdot x - 11$, where x represents the experimental binding free energy (Experimental Delta G) and y is the calculated binding free energy (Calculated Delta G) was used to predict the 100 compounds generated by BREED that were selected after pre-screening by molecular docking. Ten compounds with the highest predicted Delta G values (**Table 1**) were submitted for synthesis and biological activity evaluation. Because pan assay interference compounds (PAINS) compounds are often false positives reacting with numerous targets. They tend to react with numerous biological targets simultaneously rather than specifically affecting one desired target³¹. Thus, before further evaluation, our ten compounds were filtered through the PAINS remover (<http://cbligand.org/PAINS/>)³¹ and all passed the filtration process. The average binding free energy values for the 10 selected compounds were better (lower) or comparable to those of the ligands from the crystal structures (**Table S1** and **Figure 4b**).

Table 1 Enzymatic activity of selected compounds against VEGFR-2 as well as glide XP score and predicted Delta G obtained by molecular dynamics combined with MMPBSA.

| No. | Compound | Inhibition(%) | IC ₅₀ (nM) | Glide XP Score | Predicted Delta G (kcal/mol) |
|---------------|---|---------------|-----------------------|----------------|------------------------------|
| 6 |  | 99.71 | 15.29 | -13.50 | -17.27 |
| 7 |  | 99.05 | 28.79 | -13.25 | -15.25 |
| 8 |  | 98.9 | 17.85 | -13.53 | -14.83 |
| 10 |  | 44.31 | >10000 | -10.95 | -16.44 |
| 11 |  | 95.23 | 3937.00 | -10.20 | -12.96 |
| 19 |  | 99.79 | 0.75 | -11.90 | -15.35 |
| 20 |  | 98.74 | 0.92 | -11.07 | -13.88 |
| 21 |  | 99.5 | 1.88 | -10.97 | -12.26 |
| 22 |  | 96.5 | 8.70 | -12.47 | -12.26 |
| 23 |  | 97.78 | 33.36 | -13.88 | -17.14 |
| Sorafenib |  | 96.75 | 46.41 | -11.33 | -13.85 |
| Staurosporine | - | 99.24 | 15.97 | - | - |

* IC₅₀ values were average of three replicates.

To ensure that the simulation had reached equilibrium, RMSD and the number of protein-ligand hydrogen bonds were calculated for both the crystallized ligands and the designed compounds. The RMSD values for both the protein (**Figures 5, S1 and S3**, blue) and the ligands (**Figures 5, S1 and S3**, orange) in the 28 crystal structures and 10 target compounds were calculated, respectively. In general, the protein atoms (RMSD of 1.5–4 Å) and the ligand atoms (RMSD of 0.25–2.5 Å) reached equilibrium at approximately 2000 ps. However, among all crystal structures, protein atoms from PDB entries 1Y6A, 2OH4, 2P2I and 3DTW exhibited large fluctuations (**Figure S1**). For the ligand atoms, the crystallized ligands of PDB entries 3C7Q, 2QU6 and 4AGD fluctuated significantly (**Figure S3**). In **Figure 5**, the RMSD fluctuation of compound **6** presented a similar trend compared to the five FDA approved VEGFR-2 inhibitors including sorafenib ($IC_{50} = 90$ nM), sunitinib ($IC_{50} = 80$ nM), axitinib ($IC_{50} = 0.2$ nM), nintedanib ($IC_{50} = 21$ nM) and lenvatinib ($IC_{50} = 4$ nM) (**Table S1**). Moreover, the RMSD values for the protein atoms (PDB 3EWH) in complex with the 10 designed compounds have lower RMSD values (2 to 3 Å) than the protein atoms for the 28 crystal complexes, except the complex with compound **21** (**Figure 5 and S3**), which fluctuates from 2 to 4 Å. This observation is likely because only the most favorable crystal structure PDB 3EWH¹⁴ was adopted for docking and MD simulations for the designed compounds. The ligand RMSD values (0.25–1.5 Å) of the designed compounds fluctuated less significantly (**Figures 5 and S3**) than the crystallized ligands (0.25–2.5 Å) (**Figures 5 and S1**). Additionally, the distribution of all Delta G values calculated from the 500 snapshots (**Figure S4** for the crystal ligands and **Figure S5** for the designed compounds) followed a normal distribution, which further proved that the MD simulation reached equilibrium and the rationality of using the average Delta G value to build the prediction model.

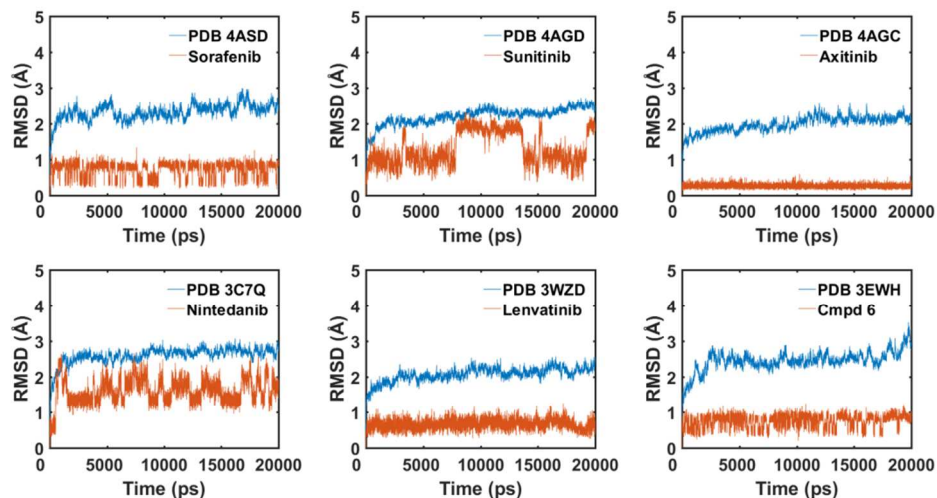


Figure 5 RMSD values during the 20 ns MD for five FDA approved drugs crystallized with VEGFR-2 protein and the designed compound **6** docked to VEGFR-2 protein (PDB 3EWH). Blue stands for the fluctuation of protein atoms and orange represents the fluctuation of ligand atoms.

Hydrogen bonding plays a vital role in protein folding, stability and function, and it is particularly important for protein-ligand binding affinity. We calculated the number of intermolecular hydrogen bonds between the protein and the compounds with respect to time. On average, the designed compounds formed more hydrogen bonds (ranged from 1 to 6, with an average of 5) during the MD simulation compared to the crystallized ligands (ranged from 0 to 6, with an average of 3) (**Figures 6, S2 and S3**). Taken together, these data indicated that the VEGFR-2 protein in complex with the designed compounds can reach an equilibrium that was comparable or better in terms of RMSD, and the complexes maintain more hydrogen bonds during the simulation. Taken together, these results indicated augmented protein stability and stronger binding of the designed compounds.

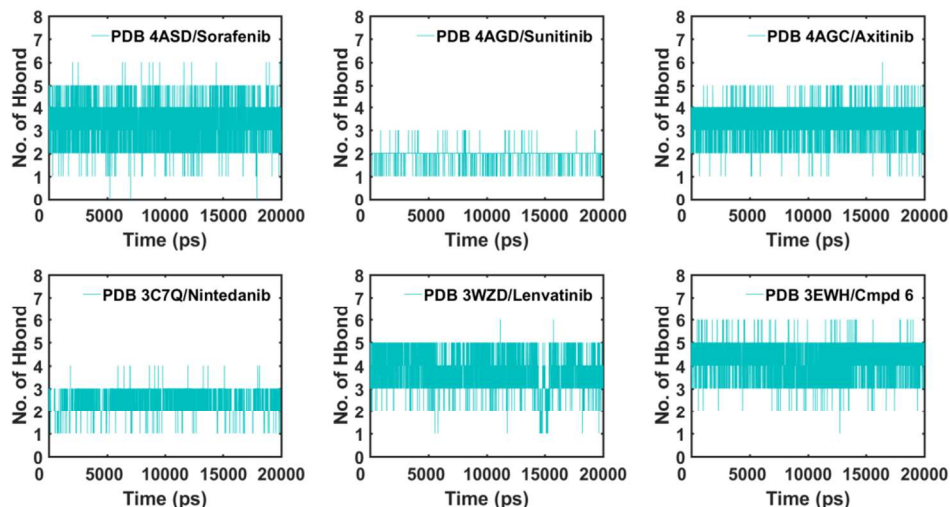
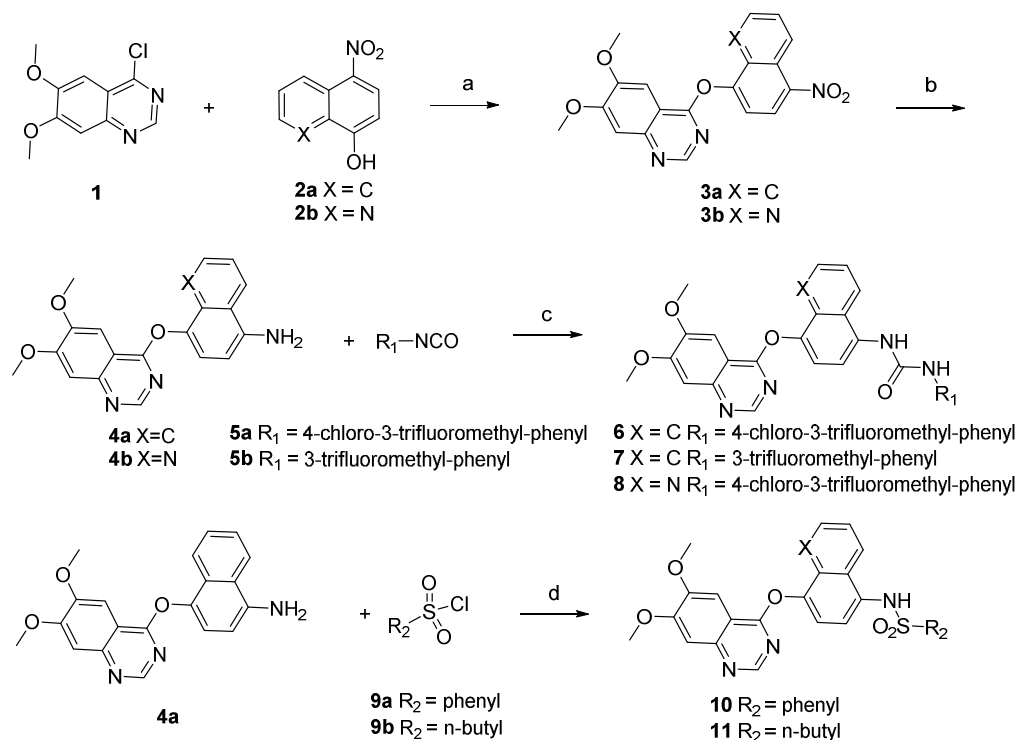


Figure 6 The number of hydrogen bonds formed during 20 ns MD simulations for five FDA approved drugs crystallized with VEGFR-2 as well as designed compound **6** docked to VEGFR-2 protein (PDB 3EWH).

Chemistry

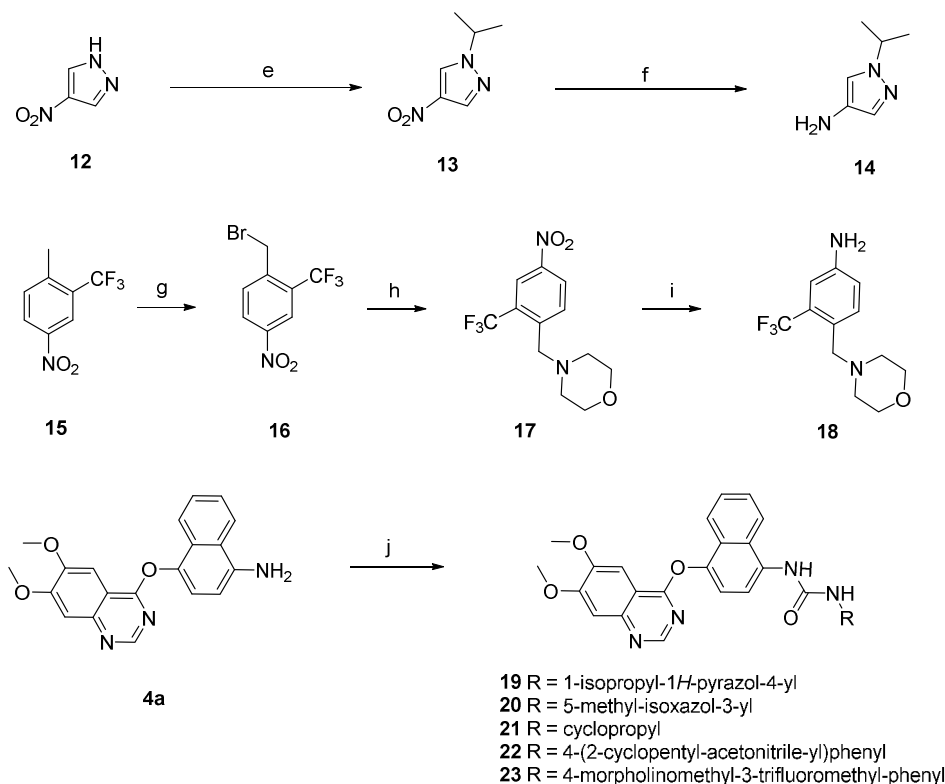
The preparation of target compounds **6**, **7**, **8**, **10** and **11** are shown on **Scheme 1**: **3a** and **3b** were obtained by nucleophilic substitution reaction of two different phenols (**2a**, **2b**) and 4-chloro-6,7-dimethoxyquinazoline (**1**). Reduction of **3a** and **3b** by iron powder provided amino compounds **4a** and **4b**. Finally, **4a** was reacted with different aryl isocyanates (**5a**, **5b**) to obtain target urea compounds **6**, **7**, and **8**. **4b** was reacted with phenylsulfonyl chloride (**9a**), and 1-butanefonyl chloride (**9b**) to obtain sulfonamides **10** and **11**, respectively.



Scheme 1 Synthesis of compounds **6**, **7**, **8**, **10** and **11**.

Reagents and conditions: (a) anhydrous DMF, NaH, 90 °C, 24 h; (b) Fe, NH₄Cl, 70% i-PrOH, 85 °C, 4 h; (c) THF, rt, 5 h; (d) THF, TEA, 0 °C - rt, 1 h/pyridine, rt, 1 h.

Preparation of target compounds **19**, **20**, **21**, **22**, and **23** are depicted on Scheme 2: **4a** was reacted with 1-isopropyl-1*H*-pyrazol-4-amine (**14**), 5-methylisoxazole-3-amine, cyclopropylamine, 1-(4-aminophenyl)cyclopentane-1-carbonitrile and 4-(morpholinomethyl)-3-(trifluoromethyl)aniline (**18**) to obtain compounds **19**, **20**, **21**, **22**, and **23**, respectively. The key intermediate **14** was prepared by Pd/C-catalyzed reduction of **13**, where **13** was obtained from nucleophilic substitution of 4-nitro-1*H*-pyrazole and 2-bromopropane. The key amine **18** was synthesized by hydrogenation of compound **17**, which was obtained by nucleophilic substitution of 4-nitro-2-(trifluoromethyl)benzyl bromide (**16**). Compound **16** was obtained from the bromination of 1-methyl-4-nitro-2-trifluorotoluene.



Scheme 2 Synthesis of compounds **19**, **20**, **21**, **22** and **23**. *Reagents and conditions:* (e) 2-bromopropane, K_2CO_3 , DMF, 50 °C, 0.5 h; (f) 20% Pd/C, H_2 , ethyl acetate, rt, 5-7 h; (g) NBS, AIBN, 1,2-dichloroethane, 90 °C, 12 h; (h) morpholine, K_2CO_3 , rt, 16 h; (i) 20% Pd/C, H_2 , EtOH, rt, 2 h; (j) (**19**) 4-nitrophenyl carbonochloridate, DCM, RNH_2 pyridine, rt, 24 h; (**20**, **21**, **22**, **23**) triphosgene, DCM, TEA, RNH_2 , 0 °C-rt, 24 h.

VEGFR-2 Kinase Activity

The inhibitory activity of the 10 target compounds was tested at 10 μM and for the compounds with inhibition ratios greater than 50 %, the VEGFR-2 IC_{50} values were investigated. The activity results (**Figure 7** and **Table 1**) showed that the VEGFR-2 inhibitory activities of the 10 target compounds at 10 μM were excellent, where nine compounds obtained an inhibition ratio above 90 %. Moreover, rescreening results showed that these nine compounds achieved nanomolar VEGFR-2 IC_{50} values. All nine compounds except compound **10** ($IC_{50} > 10000$ nM)

1
2
3 and **11** ($IC_{50} = 3937$ nM) exhibited better inhibitory activity than the positive control sorafenib
4 ($IC_{50} = 46.41$ nM). Moreover, the best three compounds, **19** ($IC_{50} = 0.75$ nM), **20** ($IC_{50} = 0.92$
5 nM) and **21** ($IC_{50} = 1.88$ nM), were more active than the other positive control staurosporine
6 ($IC_{50} = 15.97$ nM). Compound **22** ($IC_{50} = 8.7$ nM) also showed better inhibitory activity than
7 sorafenib via the introduction of a cyclopentanecarbonitrile group similar to that of apatinib,
8 which was approved for clinical use in late-stage gastric carcinoma in China by the China Food
9 and Drug Administration (CFDA) in 2016³². Enzymatic activity testing corroborated the binding
10 mode prediction, because all compounds bound to a DFG-out conformation and formed key
11 hydrogen bonds with Cys919 in the hinge region and Glu885 and Asp1046 in the hydrogen bond
12 favorable region (**Figure 8**). In addition, the bicyclic group (naphthamide or quinoline) fit
13 Hydrophobic Region I better than the monocyclic groups, and differentially substituted six-, five-
14 or three membered rings matched well with hydrophobic region II (**Figure 8a**).

15
16
17
18
19
20
21
22
23
24
25
26
27
28
29
30
31 Based on activity data, the structure activity relationship (SAR) can be summarized as follows.
32
33 First, the introduction of a naphthalene ring and a quinoline ring in Hydrophobic Region I has
34 little effect on the inhibitory activity; for example, compounds **6** and **8** exhibited inhibitory
35 activities of 15.29 and 17.85 nM, respectively. Next, Hydrophobic Region II can accommodate
36 hydrophobic groups of different sizes, such as the cyclopropyl substituent of compound **21** and
37 the substituted five-membered ring (pyrazole or oxazole) of compounds **19** (binding mode shown
38 in **Figure 8b**) and **20**, as well as the substituted phenyl group of compounds **6**, **7**, **8**, **22** and **23**.
39
40 Third, comparison of compounds **6** ($IC_{50} = 15.29$ nM), **7** ($IC_{50} = 28.79$ nM), and **23** ($IC_{50} = 33.36$
41 nM) indicated that 4-chloro substituted phenyl groups in Hydrophobic Region II did not affect
42 inhibitory activity against VEGFR-2, whereas removal or replacement with a hydrophilic
43 morpholino moiety only decreased the activity about 2-fold. Finally, replacement of the urea
44
45
46
47
48
49
50
51
52
53
54
55
56
57
58
59
60

group in the hydrogen bond acceptor or donor substituents was favored over a sulfonamide moiety (which may reduce inhibitory activity). This trend can be seen when comparing compound **6** ($IC_{50} = 15.29$ nM) with compound **10** (inhibition ratio of 44.31 %) and compound **11** ($IC_{50} = 3937$ nM), indicating that the hydrogen bond formation with Glu885 which is important for inhibitor binding may have been disrupted (**Figure 8c**)²⁸.

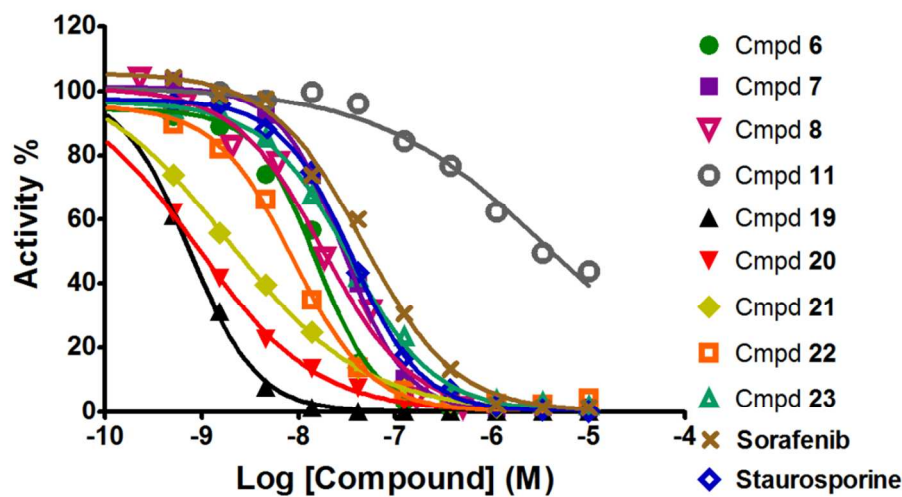


Figure 7 The dose-dependent enzymatic activity of the 10 target compounds against VEGFR-2. Results were average of three replicates.

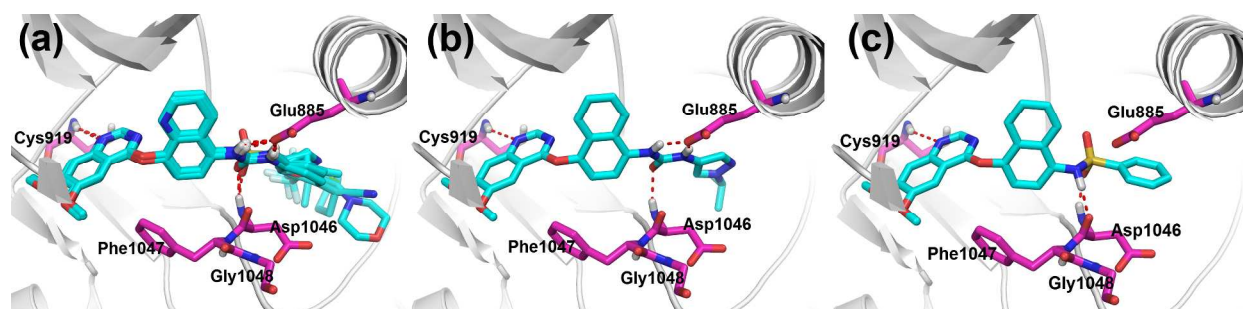


Figure 8 Binding conformation of the 10 designed compounds. (a) All 10 compounds; (b) compound **19**; and (c) compound **10**.

Based on the enzymatic activity data, the protein and ligand stability during the MD simulation process for the most active compound **19** ($IC_{50} = 0.75$ nM, colored black in **Figure 9**)

and the second least active compound **11** ($IC_{50} = 3937$ nM, colored red in **Figure 9**) was further evaluated. As illustrated in **Figure 9**, the RMSD values for the VEGFR-2 protein (PDB 3EWH) were nearly the same for the two compounds (**Figure 9a**), although for compound **19** the RMSF averaged about 1.75 Å and compound **11** averaged 2.4 Å (**Figure 9c**). Nevertheless, compound **19** reached equilibrium around 0.5 Å, while **11** obtained stability around 1 Å (**Figure 9b**). Furthermore, **19** achieved an average of 5 hydrogen bonds, while compound **11** only averaged 3 (**Figure 9d**). These results may help explain the huge loss in binding affinity for compound **11** compared to compound **19**.

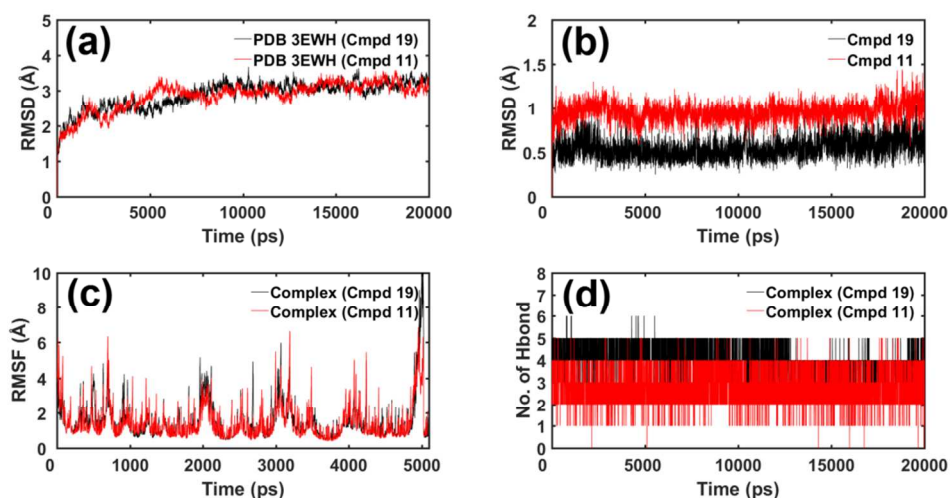


Figure 9 The RMSD (a and b), RMSF (c) and the number of hydrogen bonds (d) of the protein and ligands in the MD simulations for the most active compound **19** ($IC_{50} = 0.75$ nM, black) and the second least active **11** ($IC_{50} = 3937$ nM, red). 1 nm is equal to 10 Å.

Cellular VEGFR-2 Assays

Based on their outstanding VEGFR-2 inhibitory activity, eight compounds were submitted for initial cell proliferation inhibition activity testing. Herein, using CellTiter-Glo (CTG) cell growth inhibition test module, the growth inhibitory effect of the eight compounds on three cell lines (HUVECs³³, melanoma cell line MDA-MB-435³⁴ and epidermal squamous cell carcinoma cell

1
2
3 line A431³⁵) were measured. VEGFR-2 overexpression was found in HUVECs and MDA-MB-
4
5 435 cells in angiogenesis-related cancers³⁶. HUVECs, derived from the endothelium of veins
6
7 from the umbilical cord, are the most commonly studied human endothelial cell type in
8
9 angiogenesis³³. It has been proven that inhibiting VEGF-induced VEGFR-2 activation by small
10
11 molecules in HUVECs can inhibit subsequent angiogenesis³⁷. Here, MDA-MB-435 was used as
12
13 a melanoma cell line rather than a model for human breast cancer, because recent advances in
14
15 gene expression analysis revealed that the pattern of gene expression for MDA-MB-435 more
16
17 closely resembled that of melanoma cell lines than other breast tumor lines³⁴. Moreover, the
18
19 results from an immunofluorescence staining study showed strong VEGFR-2 staining in MDA-
20
21 MB-435 tumors³⁶. Epidermal squamous cell carcinoma cell line A431 is an epidermal growth
22
23 factor receptor (EGFR) overexpressing cell, but it can also lead to angiogenesis, which was used
24
25 as a negative control for comparison³⁸.
26
27
28
29

30
31 As shown in **Table 2**, all compounds showed good inhibitory effects against HUVECs with
32
33 compounds **19**, **22** and **23** reaching inhibition ratios of 93.58, 92.48 and 97.11 %, respectively,
34
35 which are superior to positive control sorafenib (84.66 %). At 82.89 % inhibition, compound **6**
36
37 exhibited comparable inhibitory activity to sorafenib. The inhibitory effects on the MDA-MB-
38
39 435 cell line for compounds **6**, **22** and **23** were 95.06, 96.90 and 98.36 %, respectively, also
40
41 outperforming sorafenib (91.89 %). As expected, this series of compounds did not exhibit good
42
43 inhibitory effects against the A431 cell line, which has EGFR overexpression rather than
44
45 VEGFR-2. For the A431 cell line, compounds **22** (49.05 %) and **23** (57.71 %), which obtained
46
47 the highest inhibitory activity, were still weaker than sorafenib (68.94 %). Compounds with
48
49 cellular inhibition rates greater than 90 % were further tested to obtain IC₅₀ values. As depicted
50
51 in **Figure 10** and **Table 2**, the IC₅₀ values for compounds **6**, **19**, **22** and **23** against HUVECs
52
53
54
55
56
57
58
59
60

were 2.97, 0.63, 3.62 and 0.63 μM , respectively, which is comparable with sorafenib (1.49 μM). The IC_{50} values for compounds **6**, **22** and **23** against MDA-MB-435 were 3.79, 3.01 and 2.36 μM , respectively, also comparable with sorafenib (2.11 μM). These results demonstrated that the designed compounds exhibited excellent cellular inhibitory activity, which most likely resulted from the inhibition of VEGFR-2 and were promising hits for developing antitumor candidates.

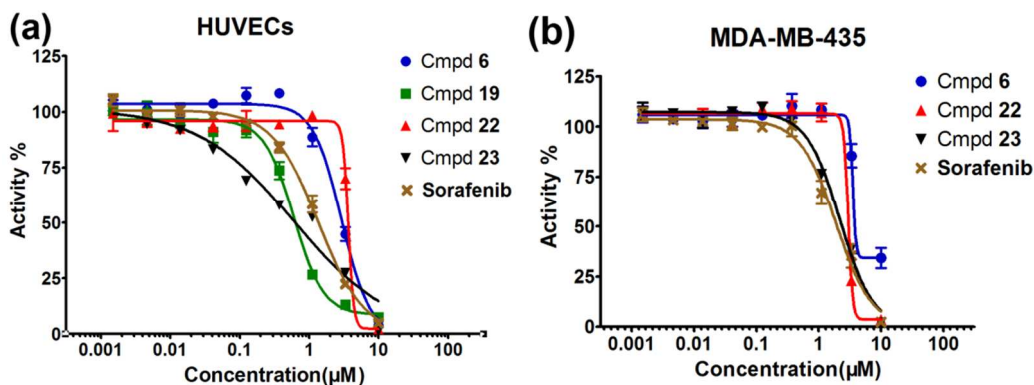


Figure 10 Cellular activity against two cell lines. (a) HUVECs and (b) MDA-MB-435 cell line. Results were from three replicates.

Table 2 Cellular inhibitory rates of eight compounds against HUVECs, MDA-MB-435 and A431 cell lines as well as IC_{50} values for four compounds for two cell lines (HUVECs and MDA-MB-435).

| No. | Cell inhibitory activity | | | | |
|-----------|--|---------------|--------|--|------------------|
| | Cell inhibition rate at 10 μM | | | IC_{50} values, μM | |
| | HUVECs | MDA-MB-435 | A431 | HUVECs | MDA-MB-435 |
| 6 | 82.89% | 95.06% | 14.95% | 2.97±0.18 | 3.79±0.93 |
| 7 | 66.8% | 24.54% | -4.51% | ND | ND |
| 8 | 51.45% | 44.29% | 20.96% | ND | ND |
| 19 | 93.58% | 27.71% | 49.87% | 0.63±0.05 | ND |

| | | | | | |
|------------------|---------------|---------------|--------|------------------|------------------|
| 20 | 61.89% | 0.23% | -1.52% | ND | ND |
| 21 | 63.9% | 1.48% | 15.13% | ND | ND |
| 22 | 92.48% | 96.90% | 49.05% | 3.62±0.17 | 3.01±0.03 |
| 23 | 97.11% | 98.36% | 57.71% | 0.63±0.02 | 2.36±0.09 |
| Sorafenib | 84.66% | 91.89% | 68.94% | 1.49±0.08 | 2.11±0.04 |

*The data in bold are compounds with cellular inhibition greater than 80 %, which were tested for corresponding IC₅₀ values. Results were from three replicates.

The anti-tumor spectrum of representative compounds

Based on cellular activity, four compounds **6**, **19**, **22** and **23** exhibited good inhibitory activity against HUVECs and the MDA-MB-435 cell line. Thus, to expand the spectrum of tumor cells tested, these four compounds were submitted to the NCI for testing in a panel of 58 cell lines (termed NCI-60). These cell lines correspond to nine tumor types including leukemia, NSCLC, colon cancer, central nervous system (CNS) cancer, melanoma, ovarian cancer, renal cancer, prostate cancer and breast cancer (shown **Figures S6–S10**). The cell lines within the NCI-60 panel of human tumor cell lines are some of the most extensively characterized cell lines in broad laboratory use and the 58 cell lines tested in this work are VEGFR-2 expressing or overexpressing ones.

As seen in **Table 3** and **Figure 11**, compound **6** had moderately potent antiproliferative activity against melanoma, renal, breast and CNS cancers. It exhibited about 50 % cell growth for at least one of the cell types that may contribute to those tumors, which means that more than 50 % of the cells were inhibited. Compound **19** did not show any antiproliferative activity to all tested cell lines, because all cell growth proportions were higher than 70 %. Compound **22** exhibited excellent antiproliferative activity against NSCLC [cell growth: A549/ATCC (25.6 %),

HOP-92 (-39.8 %) and NCI-H460 (19.3 %)], CNS cancer [cell growth: SF-268 (27 %), SF-295 (13.7 %) and U251 (-49.3 %)], ovarian cancer [cell growth: OVCAR-4 (-1.3 %), OVCAR-8 (0.6 %)], renal cancer [cell growth: 786-0 (-40.7 %), ACHN (29.3%), RXF 393 (15 %), SN12C (21.3 %) and TK-10 (24.1 %)] and breast cancer [cell growth: HS 578T (29.6 %)]. Compound **23** demonstrated the best antiproliferative activity among all four compounds. It exhibited very potent antiproliferative activity on 51 out of 58 cell lines, where the growth percent was less than 50 % (with 11 less than 0) and the average growth percent for all 58 cell lines was approximately 19.2 %, indicating that **23** can inhibit about 80 % of cell growth on all 51 cell lines on average.

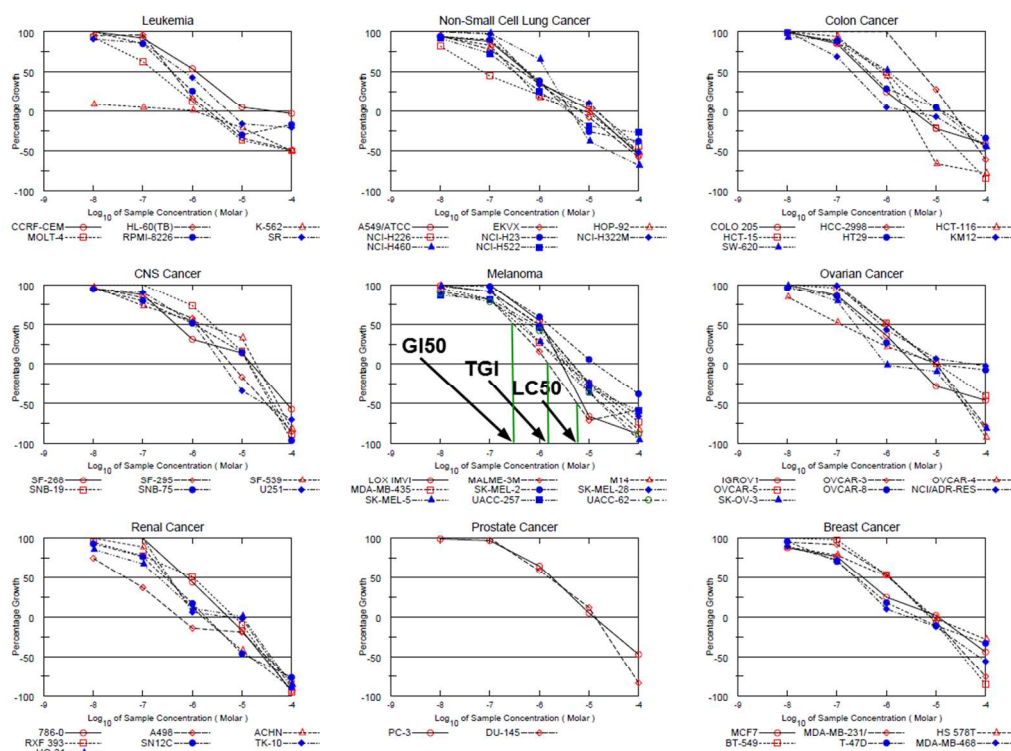


Figure 11 Dose-dependent growth inhibition curves for compound **23** on 58 cell lines conducted by NCI. A growth percent of 100 is the growth seen in untreated cells, while growth percent of 0 corresponds to no net growth during the assay and growth percent of -100 indicates the time when all cells are killed. Three endpoints are routinely calculated: (1) GI₅₀, the drug concentration yielding a growth percent of 50 (i.e., 50% growth inhibition); (2) TGI (total

growth inhibition), the concentration resulting in a growth percent of 0; (3) LC₅₀, the concentration when a growth percent of -50, or lethality in 50% of the starting cells is shown. These endpoints are illustrated for one of the melanoma cell lines MALME-CM (red open diamond).

Therefore, compound **23** was selected to determine GI₅₀ values at five concentrations with 1 log dilutions from 10⁻⁴ M to 10⁻⁸ M (**Figure 11**). Three endpoint values, GI₅₀, TGI and LC₅₀, were calculated (**Figure 11**). As illustrated in **Figure 11**, compound **23** exhibited dose-dependent inhibition behavior against all 58 cell lines, corroborating all in vitro tests. According to **Table 3**, **Figures 11 and S9**, compound **23** displayed excellent antiproliferative activity, with the GI₅₀ values against all 58 cell lines at less than 5.25 μM and TGI less than 58.9 μM. Specifically, compound **23** exhibited GI₅₀ values less than 200 nM against seven cancer cell lines including leukemia [cell lines K-562 (GI₅₀ < 10 nM) and MOLT-4 (GI₅₀ = 190 nM)], NSCLC [cell line NCI-H226 (GI₅₀ < 70 nM)], colon cancer [cell line KM12 (GI₅₀ < 200 nM)], ovarian cancer [cell line OVCAR-4 (GI₅₀ < 120 nM)], renal cancer [cell lines A498 (GI₅₀ < 50 nM) and UO-31 (GI₅₀ < 200 nM)].

Table 3 Cellular growth inhibition values of compound **23** on 58 cell lines (performed by NCI).

| Tumor type | Cell line | GI ₅₀ ^a (μM) | TGI ^b (μM) | LC ₅₀ ^c (μM) | Tumor type | Cell line | GI ₅₀ ^a (μM) | TGI ^b (μM) | LC ₅₀ ^c (μM) |
|------------|-----------|---------------------------------------|--------------------------|---------------------------------------|------------|------------|---------------------------------------|--------------------------|---------------------------------------|
| Leukemia | CCRF-CEM | 1.17 | 40.74 | >100 | Melanoma | M14 | 0.95 | 4.57 | 26.92 |
| | HL-60(TB) | 0.38 | 2.14 | >100 | | MDA-MB-435 | 0.37 | 3.39 | 33.88 |
| | K-562 | < 0.01 | 1.12 | 95.50 | | SK-MEL-2 | 1.48 | 13.80 | >100 |
| | MOLT-4 | 0.19 | 1.82 | >100 | | SK-MEL-28 | 0.89 | 4.79 | 42.66 |
| | RPMI-8226 | 0.39 | 2.95 | >100 | | SK-MEL-5 | 0.45 | 2.69 | 16.98 |
| | SR | 0.69 | 5.37 | >100 | | UACC-257 | 0.79 | 3.98 | 47.86 |

| | | | | | | | | | |
|-----------|-----------|-------------|-------|--------------|----------|---------------------|-------------|-------|-------|
| | A549/ATCC | 0.55 | 10.72 | 81.28 | | UACC-62 | 0.60 | 3.47 | 18.62 |
| | EKVX | 0.45 | 6.46 | 67.61 | | IGROV1 | 0.52 | 3.63 | >100 |
| | HOP-92 | 0.32 | 7.76 | 91.20 | | OVCAR-3 | 1.00 | 9.55 | 42.66 |
| Non-small | NCI-H226 | 0.07 | 13.80 | >100 | Ovarian | OVCAR-4 | 0.12 | 10.47 | 35.48 |
| cell lung | NCI-H23 | 0.62 | 3.98 | >100 | cancer | OVCAR-5 | 1.07 | 10.47 | >100 |
| cancer | NCI-H322M | 0.56 | 15.14 | 93.33 | | OVCAR-8 | 0.40 | 9.55 | >100 |
| | NCI-H460 | 1.41 | 4.27 | 25.70 | | NCI/ADR- RES | 0.76 | 58.88 | >100 |
| | NCI-H522 | 0.31 | 3.80 | >100 | | SK-OV-3 | 0.23 | 0.95 | 37.15 |
| | COLO 205 | 0.38 | 3.39 | >100 | | 786-0 | 0.79 | 5.37 | 26.92 |
| | HCC-2998 | 5.25 | 20.89 | 75.86 | | A498 | 0.05 | 0.52 | 30.90 |
| Colon | HCT-116 | 0.79 | 2.57 | 7.08 | Renal | ACHN | 0.32 | 1.62 | 14.13 |
| cancer | HCT-15 | 1.00 | 5.13 | 28.18 | cancer | RXF 393 | 1.05 | 7.08 | 29.51 |
| | HT29 | 0.45 | 13.18 | >100 | | SN12C | 0.29 | 1.86 | 13.18 |
| | KM12 | 0.20 | 2.51 | >100 | | TK-10 | 0.38 | 5.89 | 35.48 |
| | SW-620 | 1.10 | 11.75 | >100 | | UO-31 | 0.20 | 10.23 | 38.02 |
| | SF-268 | 0.46 | 15.85 | 79.43 | Prostate | PC-3 | 1.78 | 12.59 | >100 |
| | SF-295 | 1.23 | 6.03 | 30.90 | Cancer | DU-145 | 1.55 | 13.18 | 44.67 |
| | SF-539 | 1.58 | 19.50 | 52.48 | | MCF7 | 0.33 | 10.96 | >100 |
| CNS | SNB-19 | 2.57 | 14.13 | 43.65 | | MDA-MB- 231/ATCC | 1.15 | 7.94 | 42.66 |
| cancer | SNB-75 | 1.05 | 13.80 | 38.90 | Breast | HS 578T | 1.12 | 9.33 | >100 |
| | U251 | 1.05 | 3.98 | 27.54 | cancer | BT-549 | 1.15 | 7.41 | 34.67 |
| | LOX IMVI | 1.10 | 2.82 | 7.24 | | T-47D | 0.25 | 4.27 | >100 |
| Melanoma | MALME-3M | 0.30 | 1.55 | 5.75 | | MDA-MB-468 | 0.23 | 2.82 | 72.44 |

The description of ^aGI₅₀, ^bLC₅₀, ^cTGI are the same as **Figure 11**. GI₅₀ values less than 1 μM or LC₅₀ values higher than 100 μM are shown in bold.

In addition, the NCI-60 results of compound **23** were compared with the results for two FDA

1
2
3 approved VEGFR-2 drugs sorafenib and sunitinib, which were downloaded from
4 https://dtp.cancer.gov/discovery_development/nci-60/. Sorafenib, a Raf-VEGFR-2 dual inhibitor,
5
6 https://dtp.cancer.gov/discovery_development/nci-60/. Sorafenib, a Raf-VEGFR-2 dual inhibitor,
7 is now used for renal cell carcinoma, hepatocellular carcinoma and thyroid cancer treatments¹⁶.
8
9 Sunitinib³⁹ is used for the treatment of renal cell carcinoma, pancreatic neuroendocrine tumors,
10 and gastrointestinal stromal tumors to complement intolerance to imatinib¹⁶. The comparison of
11 the mean endpoint values for all cell lines to each tumor is shown in **Figure 12** and the original
12 GI₅₀, TGI and LC₅₀ values for each cell line are displayed in **Figures S11-S13**, respectively.
13
14 Based on **Figure 12**, although only the renal cancer cell line that is approved for both drugs was
15 included in the NCI-60, we observed that the GI₅₀ values of compound **23** were 9.5- and 6.8-fold
16 better (lower) than those of sorafenib and sunitinib, respectively. The TGI values were both 3.2-
17 fold lower than the two marketed drugs. In addition, the LC₅₀ values were 2 and 1.3-fold worse
18 (higher) than these drugs, respectively, indicating that compound **23** was more potent in the cell
19 lines responsible for renal cancer, and its safety was comparable with that of sorafenib and
20 sunitinib for clinical use in renal cancer. For the other eight tumor types, compound **23** exhibited
21 higher potency against the cell lines and was more safe or comparable to sorafenib and sunitinib.
22 Specifically, its GI₅₀ values were at least 3.9–9.5-fold and 5–7.7-fold better than sorafenib and
23 sunitinib, respectively, for leukemia, NSCLC, ovarian cancer and breast cancer. For colon cancer,
24 CNS cancer, melanoma and prostate cancer, the GI₅₀ of compound **23** was about 1.6–2.9-fold
25 and 1.1–3.7-fold better than that of sorafenib and sunitinib, respectively. Among all cancers,
26 renal and ovarian cancers are VEGF/VEGFR pathway inhibitor-sensitive (such as VEGF
27 antibodies and VEGFR-2 TKIs) tumors, while NSCLC, breast cancer and colon cancer are only
28 partly sensitive to VEGFR inhibitors.¹⁶ Among the cell lines tested, NCI/ADR-RES is a
29 multidrug-resistant cancer cell line for ovarian cancer⁴⁰. Nevertheless, compound **23** exhibited
30
31
32
33
34
35
36
37
38
39
40
41
42
43
44
45
46
47
48
49
50
51
52
53
54
55
56
57
58
59
60

very strong antiproliferative activity with a GI_{50} of about 0.76 μ M, which is 3.3- and 6.9-fold better than sorafenib and sunitinib, respectively (**Figure S11**), demonstrating that this compound may inhibit some drug-resistant cell lines.

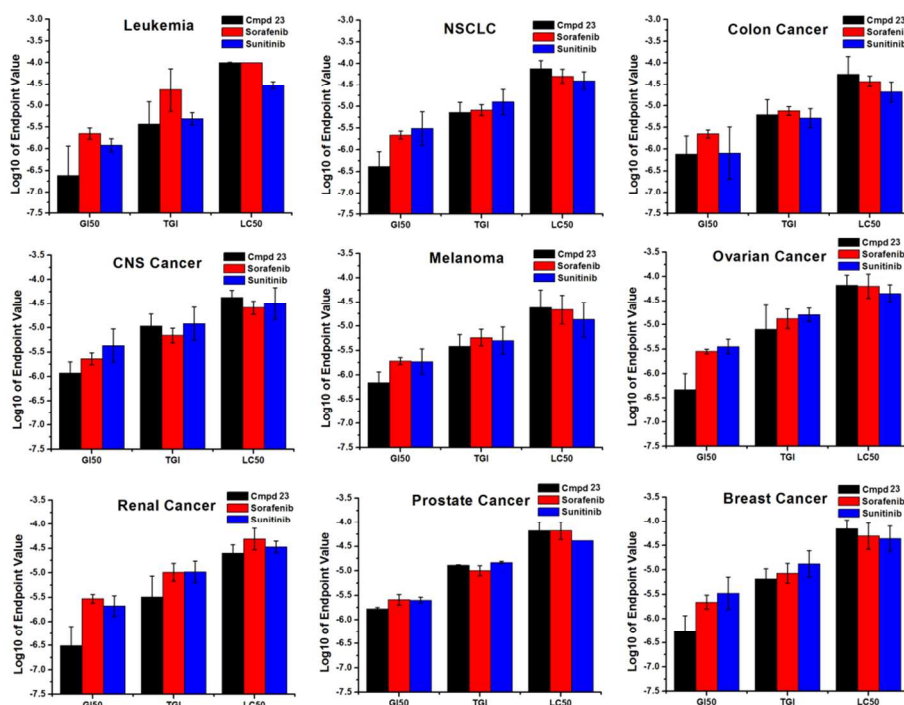


Figure 12 Comparison of the GI_{50} , TGI and LC_{50} values for compound **23** (black), sorafenib (red) and sunitinib (blue). The y-axis is the log value of the endpoints and a difference of 1 indicates a 10-fold difference in the endpoint values.

Studies showed that increased expression of VEGF/VEGFR-2 in leukemic blasts and correlation with angiogenesis in the bone marrow of acute myeloid leukemia (AML) patients has been observed⁴¹. VEGF is also a major contributor to the growth of CNS tumors, as elevated expression of VEGF is one of the factors responsible for the virulent nature of these tumors. Thus, interruption of VEGFR signaling, specifically VEGFR-2, may effectively suppress tumor growth in leukemia and CNS cancer^{42, 43}. However, the expression of VEGFR-2 in melanoma

1
2
3 cells is controversial. Several studies have shown that high quantities (78-89%)^{44, 45} or at least
4 half of melanoma cells⁴⁶ express VEGFR-2. Others indicated that relatively few (<10%)
5 melanoma cells expressed detectable levels of VEGFR-2⁴⁷. Nevertheless, sorafenib, a dual
6 inhibitor of BRAf and VEGFR-2 with promise in other cancers driven by VEGF, was relatively
7 ineffective when used as a single agent in melanoma. Despite these studies casting doubt on
8 VEGFR-2 as an effective target in melanoma, the identification of VEGFR-2 positive melanoma
9 cell lines still presents an opportunity to personalize therapy using antibodies and other TKIs that
10 specifically target VEGFR-2-dependent signaling. All data implied that the inhibition of the cell
11 lines by compound **23** probably stems from its inhibition of VEGFR-2 rather than an off-target
12 effect. Nevertheless, because compound **23** was a multikinase inhibitor, which we will discuss
13 later, the inhibition of the cell lines may also benefit from activity at other targets. For example,
14 sorafenib is the only compound used for the treatment of hepatocellular carcinoma among the
15 VEGFR-2 related approved drugs. It is probably because of positive clinical trial results in
16 hepatocellular carcinoma, which may be due to its BRAf inhibitory activity as the overexpression
17 of BRAf was indeed frequently observed in hepatocellular carcinoma. However, further efforts to
18 understand the complete role of sorafenib in the treatment of hepatocellular carcinoma and the
19 cell antiproliferative activity of compound **23** are still necessary.

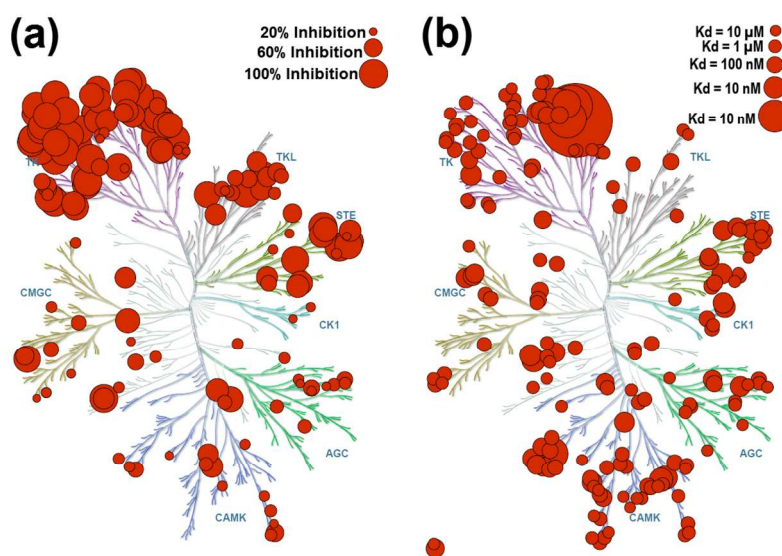
20
21
22
23
24
25
26
27
28
29
30
31
32
33
34
35
36
37
38
39
40
41
42 As the second leading cause of male cancer death in developed countries, prostate cancer
43 belongs to one of the VEGF/VEGFR pathway inhibitor resistant cancers¹⁶. The expression of
44 VEGFRs in endothelial cells isolated from prostate tumors has confirmed this finding. However,
45 though sunitinib and sorafenib showed similar anti-angiogenic and cytotoxic effects on normal
46 endothelial cells, sunitinib affected the proliferation, survival and motility of prostate tumors,
47 whereas sorafenib only showed a minor effect. Both medications inhibited VEGFR-2
48
49
50
51
52
53
54
55
56
57
58
59
60

1
2
3 phosphorylation of prostate cancer endothelial cells, while they differentially modulated Akt
4 phosphorylation, as no inhibitory effect of sorafenib was observed on Akt activation⁴⁸. The
5 combined treatment with Casodex reverted the observed resistance to sorafenib both on cell
6 viability and on Akt activation, whereas it did not modify the response to sunitinib. Thus, the
7 mechanism for the activity of sunitinib on prostate cancer remains unknown. Compound **23**
8 exhibited about 1.6- and 1.5-fold better GI₅₀ than sorafenib and sunitinib on prostate cancer,
9 respectively (**Figure 12**). Compound **23** TGI and LC₅₀ were similar to that of those two FDA-
10 approved drugs. Specifically, the LC₅₀ value of compound **23** was 1.7-fold of sunitinib, showing
11 a safer effect. However, its inhibition of Akt was not obvious (less than 20% on VEGFR-2
12 inhibition at 10 μM). Nevertheless, the resistance of prostate cancer to VEGF inhibitors is more
13 likely related to redundancy in angiogenic pathways. A large amount of data indicates that
14 fibroblast growth factor (FGF) and its family of receptors (FGFRs) were observed in the
15 transformation and angiogenesis of prostate cancer, and several early-phase clinical trials are
16 assessing FGFR TKIs in this disease¹⁶. Thus, there is a possibility that compound **23** works in a
17 similar way, as it showed higher than 96% inhibition on FGFR-1/-2/-3/-4. Therefore, we cannot
18 jump to any conclusions about whether this compound is a powerful prostate cancer hit, but it
19 still holds promise for further evaluation as a potential candidate like sunitinib⁴⁸.

20 21 22 **Kinome spectrum screening.**

23 To further investigate compound efficacy, compound **23** was evaluated at 0.5 μM against the
24 Reaction Biology Corporation broad kinase spectrum panel containing 349 therapeutically
25 important kinases (**Figure 13**). The kinome phylogenetic tree was generated using
26 KinomeRender⁴⁹. **Figure 13a** illustrates that compound **23** was a potent multi-targeted kinase
27 inhibitor, particularly for tyrosine kinase (TK) branch including targets like members of the
28
29
30
31
32
33
34
35
36
37
38
39
40
41
42
43
44
45
46
47
48
49
50
51
52
53
54
55
56
57
58
59
60

1
2
3 VEGFR, Abl, DDR, EPHA, FGFR, Flt, and PDGFR families as well as the STE family
4 including KHS, TNIK and HCK (**Figure 13b**), TAK1 of the TKL family and SLK of the CAMK
5 family. The kinase inhibition profile of compound **23** was similar to that of FDA approved
6 sunitinib²¹ (**Figure 13**). Through a multiple sequence alignment, we discovered that the targets
7 such as Src, PDGFR and FGFR for which compound **23** exhibited high inhibition also had higher
8 sequence identity. About two-third (38 out of 56) of the targets with inhibition greater than 90%
9 were found in the 105 targets exhibiting high sequence identity (greater than 30%) with VEGFR-
10 2 (**Table S2**). This thus indicated that the selectivity profile can be determined by sequence
11 identity. This was consistent with a comparison of multi-target drugs that inhibited target pairs in
12 the human kinome, particularly the receptor tyrosine kinase family, with combination drugs that
13 are able to inhibit targets of distant homology relationship⁵⁰. Compound **23**, a multi-targeted
14 kinase inhibitor, is likely to inhibit multiple targets simultaneously, which may overcome any
15 resistance mechanism that involves bypass or restoration of persistent mitogen-activated protein
16 kinase (MAPK) activation. However, compound **23** may also impart unwanted off-target side
17 effects, which necessitates further optimization and compound evaluation.



1
2
3 **Figure 13.** The kinome phylogenetic trees of **23** and sunitinib. (a) Percent inhibition by **23**
4 against all 349 therapeutically important kinases. (b) K_d values of sunitinib. The AGC branch
5 contains the PKA, PKG and PKC families; CAMK is calcium/calmodulin-dependent protein
6 kinase; CK1 is casein kinase 1; the CMGC branch contains the CDK, MAPK, GSK3 and CLK
7 families; STE refers to homologs of yeast Sterile 7, Sterile 11 and Sterile 20 kinases; TK is
8 tyrosine kinase; and TKL corresponds to tyrosine kinase-like proteins.
9
10
11
12
13
14
15
16
17

18 Protein kinases are the second-most investigated drug target group after G-protein-coupled
19 receptors (GPCRs), which account for 30% of drug discovery projects at many pharmaceutical
20 companies with dozens of compounds in clinical development⁵¹. However, due to highly similar
21 ATP binding pockets, kinase selectivity of drugs has become one of the greatest challenges in
22 drug discovery. Since multiple signaling pathways are involved in most tumors, many of the
23 inhibitors in clinical development are designed to affect multiple targets. Among the 46 FDA
24 approved drugs targeting the human kinome, 15 are multitarget drugs and 14 are approved for
25 use in combination with other drugs⁵⁰. Seven of the nine VEGFR-2 involved FDA approved
26 drugs (sorafenib, sunitinib, vandetanib, regorafenib, cabozantinib, nintedanib and lenvatinib) are
27 also multitarget drugs, demonstrating the effectiveness of designing multitarget inhibitors
28 involving VEGFR-2.
29
30
31
32
33
34
35
36
37
38
39
40
41
42

43 The initial effort in developing multitarget drugs stems from a belief that attacking more than
44 one target can provide better efficacy and safety profiles compared to single target drugs. At
45 present, there are two contrasting multitarget drug discovery strategies. The first method focuses
46 on discovering agents that can simultaneously inhibit two or more targets like compound **23** that
47 we discussed herein. The second strategy involves a combination of agents that are selective for
48 a single target to achieve an additive or synergistic effect⁵². However, multitarget inhibitors from
49
50
51
52
53
54
55
56
57
58
59
60

1
2
3 the first strategy risk side effects from unwanted compensatory mechanisms. Moreover, the
4
5 multitarget inhibitors from the second strategy may be confronted with the problem of attenuated
6
7 effectiveness by pharmacokinetic variations among individual ingredients as well as drug-drug
8
9 interactions. Thus, there is a recent trend to develop more selective inhibitors, but highly
10
11 selective inhibitors still face the problem of low efficacy for treating diseases like cancer, which
12
13 might achieve compensation via redundant signaling pathways. Therefore, the development of
14
15 selectively nonselective kinase inhibitors has been proposed, which will just modulate the
16
17 cancer-related targets to strike the correct balance of the nonselectivity (promiscuity) that is
18
19 essential for efficacy and the selectivity required for safety⁵². However, a comprehensive
20
21 analysis of kinase inhibitor selectivity showed that no dedicated inhibitors exist yet²¹. In addition,
22
23 the advantages and disadvantages of multi-kinase inhibitors and single kinase inhibitors are
24
25 related to potential resistance mechanisms, pharmacokinetics, selectivity and tumor
26
27 environment⁵³. Although it is currently difficult to intentionally design a multitarget inhibitor
28
29 with activity only on the kinases of interest, increasingly rational and elegant medicinal
30
31 chemistry approaches are being implemented to solve this difficult problem.
32
33
34
35
36

37 CONCLUSIONS

38
39 In this work, computational and experimental methods are seamlessly integrated for the
40
41 discovery of a series of novel VEGFR-2 inhibitors. Specifically, a robust linear model, between
42
43 the computational and experimental binding free energy (calculated by MM/PBSA) for scoring
44
45 the potential hits, was constructed with a Pearson correlation coefficient (R) of 0.8. A total of 10
46
47 compounds with relatively high predicted binding affinity were synthesized and evaluated their
48
49 in vitro activity. Eight compounds showed nanomolar IC₅₀ values against VEGFR-2, and the best
50
51
52
53
54
55
56
57
58
59
60

1
2
3 compounds were **19** (0.75 nM) and **20** (0.92 nM). Three compounds (**6**, **22** and **23**) exhibited
4 micromolar antiproliferative effects against HUVECs and melanoma cell line MDA-MB-435.
5
6
7

8
9 Through the NCI antiproliferative activity testing against 58 cancer cell lines involving nine
10 tumor types, compounds **6** and **22** demonstrated potent antiproliferative activity against
11 numerous cell lines that are responsible for renal, breast and CNS cancers. In addition,
12 comparison of the NCI screening results with two FDA approved drugs, sorafenib and sunitinib,
13 indicated that compound **23** had better antiproliferative activity against cell lines related to all
14 nine tumor types tested in terms of GI₅₀ values. Regarding drug safety, the **23** LC₅₀ values were
15 better than or comparable with those of sorafenib and sunitinib. It even demonstrated high
16 potency in one of the drug-resistant cell lines (NCI/ADR-RES) responsible for ovarian cancer as
17 well as cell lines that contribute to prostate cancer, which is regarded as one of the
18 VEGF/VEGFR pathway drug-resistant tumors. However, the intrinsic mechanism of this
19 inhibition should be further evaluated by considering the multitarget inhibition profile of
20 compound **23**. As a multi-targeted kinase inhibitor like sunitinib, compound **23** is more likely to
21 inhibit multiple targets simultaneously, which may overcome any resistance mechanism that
22 involves bypass or restoration of persistent alternative pathway activation. Nevertheless, it may
23 also bring unwanted off-target side effects, which are difficult to predict during the drug design
24 process. In summary, because of both its efficacy and safety data, compound **23** may be a
25 promising candidate for the treatment of leukemia, NSCLC, colon cancer, ovarian cancer and
26 breast cancer. The integration of both computational and experimental studies like those
27 conducted herein can be expanded in the future to similar situations with other important targets.
28 This could be more efficiently drive drug discovery forward by leveraging computational power
29 and applying existing structural data in parallel with experimental work.
30
31
32
33
34
35
36
37
38
39
40
41
42
43
44
45
46
47
48
49
50
51
52
53
54
55
56
57
58
59
60

EXPERIMENTAL SECTION

Molecular modeling

Molecular docking

The x-ray crystal structure of human VEGFR-2 (PDB code 3EWH) was downloaded from the Protein Data Bank (PDB) and prepared using the Protein Preparation Wizard in the Schrödinger suite⁵⁴. The small molecules were initially minimized by the LigPrep module in Schrödinger. The Glide module in extra precision (XP) mode was selected for molecular docking due to its excellent performance in a self-docking analysis¹⁴, and the 10 best poses of each ligand were minimized by a post-docking program that saved the best pose for further analysis.

Binding site detection

The SiteMap⁵⁵ module in the Schrödinger software suite⁵⁴ was used to detect the active site of VEGFR-2. This incorporated SiteMap program is an accurate yet fast binding site identification tool that was used herein not only to detect the binding site of the VEGFR-2 crystal structure but also to predict the druggability of those sites⁵⁵.

BREED

Ligand hybridization is a commonly employed method in FBDD. This process generates novel inhibitors that are based on structures of known ligands, which is essentially the automation of common medicinal chemistry practice. All related crystal structures complexed with ligands are aligned and all pairs of ligands with overlapping bonds are exchanged to generate new compounds. However, crossover bonds may be restricted to bias the generated structures towards synthetic accessibility. As this method is automated, all possible combinations of known ligands are investigated and generated recursively. Therefore, this process generates four types of compounds: entirely novel scaffolds, known scaffolds with novel substituents, the same scaffolds

1
2
3 as known inhibitors not included in the initial set, and sometimes a reconstruction of the input
4 ligands. BREED was implemented in MOE software with all parameters set as the default
5 configuration.²³ All crystal structures as well as the compounds generated by BREED had
6
7
8
9
10 duplicates removed.

11 12 13 *Molecular Dynamics Simulations*

14
15 After molecular docking, the protein complexes were used for MD simulations. These MD
16 simulations were performed using GROMACS⁵⁶ with the AMBER03 force field⁵⁷ and the TIP3P
17 water model⁵⁸. The proteins were simulated in a water filled dodecahedron box with a distance of
18 at least 12 Å between the complex and the box edges. Charges were neutralized by adding
19 counter ions (either Na⁺ or Cl⁻) by the genion tool. Then, the system was relaxed through an
20 energy minimization process with the steepest descent algorithm first, followed by a conjugate
21 gradient algorithm. After that, an NVT simulation was performed with the temperature
22 increasing from 100 to 300 K, followed by an NPT simulation to equilibrate the pressure. Finally,
23 a production MD simulation was performed for 20 ns at 300 K. Bond lengths were constrained
24 using the LINCS algorithm⁵⁹. The last 5 ns of each production simulation were extracted at every
25 10 ps interval for calculating the MM/PBSA binding energy using the AMBER12 package⁶⁰.
26
27 The average energy for the 1000 snapshots, where one energy value was calculated for each one
28 of the 5, 10 ps samples (representing a total of 50 ps), was saved for further analysis⁶¹. The
29 RMSD, RMSF and the number of hydrogen bonds formed were analyzed by r_rms and g_hond
30 tools, respectively in the GROMACS package⁶².
31
32
33
34
35
36
37
38
39
40
41
42
43
44
45
46
47
48
49
50

51 **Chemistry experiments.**

52
53 General synthetic routes of the ten target compounds were provided in **Scheme 1** and **Scheme 2**.
54
55 The structures of these compounds were characterized by ¹H-NMR, IR and MS. The structural
56
57

1
2
3 information for both the intermediates and target compounds are shown below. Melting points
4 were determined by an X-4 Melting-point Apparatus with Microscope (Beijing Tech Instrument)
5 and were not corrected. ^1H NMR spectra were determined on Bruker AV300 and Bruker AM500
6 spectrometers. Chemical shifts for ^1H NMR are reported in parts per million (ppm) and
7 calibrated to the solvent peak set. MS spectra were determined by Nicolet 2000 FT-IR mass
8 spectrometer and MAT-212 mass spectrometer. IR was recorded on a SHIMADZU FTIR-8400S
9 infrared spectrometer. All the final compounds were tested by HPLC and the purity in every case
10 was $\geq 95\%$. Reverse phase HPLC was conducted on Agilent Technologies 1260 Infinity, which
11 was equipped with a C18 column (Agilent Zorbax SB-C18, 5 μm , 4.6 mm \times 150 mm). Mobile
12 phase A was water, and mobile phase B was methanol. A gradient of 20–80% B was run at a
13 flow rate of 0.8 mL/min over 30 min.
14
15
16
17
18
19
20
21
22
23
24
25
26
27

28 *6,7-Dimethyl-4-(4-nitro-1-naphthalenyloxy)-quinazoline, 3a.*

29
30 To a solution of 4-nitro-1-naphthol (1.36 g, 7.19 mmol) in dry N,N-dimethylformamide (6 mL),
31 sodium hydride (345.2 mg, 8.63 mmol, 60 % in mineral oil) was added at 0 $^\circ\text{C}$ and stirred for 30
32 min at room temperature. A solution of 4-chloro-6,7-dimethoxyquinazoline (1.6 g, 7.19 mmol) in
33 dry N,N-dimethylformamide (4 mL) was added and the reaction mixture was heated to 90 $^\circ\text{C}$ for
34 24 h. The reaction mixture was taken up in ethyl acetate and water. The organic phase was
35 washed, dried and evaporated. Recrystallization from ethyl acetate resulted in an off-white solid.
36 Yield: 950 mg (34.6 %). mp: 213-215 $^\circ\text{C}$; MS $[\text{M}+\text{H}]^+$: 378.1; ^1H -NMR[300 MHz, DMSO- d_6] δ
37 8.52-8.47 (m, 3H, ArH), 8.09 (d, $J = 8.4$ Hz, 1H, ArH), 8.09 (t, $J = 7.3$ Hz, 1H, ArH), 7.77-7.69
38 (m, 3H, ArH), 7.46 (s, 1H, ArH), 3.17 (d, $J = 5.3$ Hz, 6H, -OCH $_3$).
39
40
41
42
43
44
45
46
47
48
49
50

51 *6,7-Dimethyl-4-((5-nitro-quinoline-8-yl)-oxy)-quinazoline, 3b.*

To a solution of 8-hydroxy-5-nitroquinoline (500 mg, 2.63 mmol) in dry N,N-dimethylformamide (5 mL), sodium hydride (127 mg, 3.16 mmol, 60 % in mineral oil) was added at 0 °C and stirred for 30 min at room temperature. A solution of 4-chloro-6,7-dimethoxyquinazoline (127 mg, 2.63 mmol) in dry N,N-dimethylformamide (2 mL) was added and the reaction mixture was heated to 140 °C for 10 h. The reaction mixture was taken up in ethyl acetate and water. The organic phase was washed, dried and concentrated. The residue was purified by column chromatography on silica gel to give the title compound as a pale yellow solid. Yield: 180 mg (18.9%). MS [M+H]⁺: 347.1

4-((6,7-dimethoxyquinazolin-4-yl)oxy)naphthalen-1-amine, 4a.

To a solution of 6,7-dimethyl-4-(4-nitro-1-naphthalenyloxy)-quinazoline (**3a**) (2 g, 5.93 mmol) in 70% isopropyl alcohol (25 mL), iron powder (996.7 mg, 17.8 mmol) and ammonium chloride (635 mg, 11.87 mmol) was added at 0 °C. Then, the reaction mixture was stirred at 85 °C for 4 h. The reaction mixture was filtered and the filtrate was concentrated. The residue was purified by silica gel column chromatography to give a pale yellow solid. Yield: 1.36 g (66.06%). MS [M+H]⁺: 348.1.

8-((6,7-dimethoxyquinazolin-4-yl)oxy)quinolin-5-amine, 4b.

To a solution of 6,7-dimethoxy-4-((5-nitroquinolin-8-yl)oxy)quinazoline (**3b**) (140 mg, 0.37 mmol) in 70% isopropyl alcohol (5 mL) was added at 0 °C iron powder (82.8 mg, 1.48 mmol) and ammonium chloride (59.37 mg, 1.11 mmol). Then, the reaction mixture was stirred at 85 °C for 4 h. The reaction mixture was filtered and the filtrate was concentrated. The residue was purified by silica gel column chromatography to give the title compound. Yield: 28.0 mg (21.8%); ¹H-NMR[300 MHz, DMSO-*d*₆] δ 8.62 (d, *J* = 2.7 Hz, 1H, ArH), 8.59 (d, *J* = 8.6 Hz, 1H, ArH), 8.36

(s, 1H, ArH), 7.69 (s, 1H, ArH), 7.41–7.37 (m, 3H, ArH), 6.75 (d, $J = 8.3$ Hz, 1H, ArH), 6.02 (s, 2H, -NH₂), 4.06 (d, $J = 3.42$ Hz, 6H, -OCH₃).

1-(4-chloro-3-(trifluoromethyl)phenyl)-3-(4-((6,7-dimethoxyquinazolin-4-yl)oxy)naphthalen-1-yl)urea, 6.

4-((6,7-Dimethoxyquinazolin-4-yl)oxy)naphthalen-1-amine (**4a**) (60 mg, 0.086 mmol) and 4-chloro-3-trifluoromethylphenyl isocyanate (38.2 mg, 0.086 mmol) were dissolved in dry tetrahydrofuran (5 mL) and stirred at room temperature for 5 h. The reaction mixture was filtered and the filter cake was washed with tetrahydrofuran and dichloromethane to obtain a white solid. Yield: 41 mg (83.7%); mp: >250 °C; MS [M+H]⁺: 569.2; ¹H-NMR[300 MHz, DMSO-*d*₆] δ 9.55 (s, 1H, -NHCONH-), 8.99 (s, 1H, -NHCONH-), 8.45 (s, 1H, H-quinazoline), 8.18–8.16 (m, 2H, ArH), 7.97 (d, $J = 8.3$ Hz, 1H, ArH), 7.85–7.60 (m, 5H, ArH), 7.59–7.39 (m, 3H, ArH), 4.03 (d, $J = 3.8$ Hz, 6H, -OCH₃); IR (KBr): 3266, 1629, 1566, 1505, 1422, 1379, 1233, 1171, 1117 cm⁻¹. HPLC purity 97.3%.

1-(4-((6,7-dimethoxyquinazolin-4-yl)oxy)naphthalen-1-yl)-3-(3-(trifluoromethyl)phenyl)urea, 7.

4-((6,7-Dimethoxyquinazolin-4-yl)oxy)naphthalen-1-amine (**4a**) (200 mg, 0.58 mmol) and 3-trifluoromethylphenyl isocyanate (113 mg, 0.6 mmol) were dissolved in dry dichloromethane (5 mL) and stirred at room temperature for 5 h. The reaction mixture was filtered and the filter cake was washed with tetrahydrofuran and dichloromethane to obtain a light brown solid. Yield: 236 mg (76.1%); mp: 231–235 °C; MS [M+H]⁺: 557.2; ¹H-NMR[300 MHz, DMSO-*d*₆] δ 9.44 (s, 1H, -NHCONH-), 8.95 (s, 1H, -NHCONH-), 8.45 (s, 1H, H-quinazoline), 8.21 (d, $J = 8.5$ Hz, 1H, ArH), 8.11 (s, 1H, H-quinazoline), 8.01 (d, $J = 8.2$ Hz, 1H, ArH), 7.80–7.76 (m, 2H, ArH), 7.69–7.67 (m, 2H, ArH), 7.64–7.43 (m, 4H, ArH), 7.35 (d, $J = 7.6$ Hz, 1H, ArH), 4.03 (d, $J = 3.8$ Hz,

6H, -OCH₃); IR (KBr): 3266, 1629, 1566, 1505, 1422, 1379, 1233, 1171, 1117 cm⁻¹. HPLC purity 99.3%.

1-(4-chloro-3-(trifluoromethyl)phenyl)-3-(8-((6,7-dimethoxyquinazolin-4-yl)oxy)quinolin-5-yl)urea, **8**

8-((6,7-Dimethoxyquinazolin-4-yl)oxy)quinolin-5-amine (**4b**) (42 mg, 0.12 mmol) and 4-chloride-3-trifluoromethylphenyl isocyanate (26.6 mg, 0.12 mmol) were dissolved in tetrahydrofuran (5 mL) and stirred at room temperature for 5 h. The reaction mixture was filtered and the filter cake was washed with tetrahydrofuran and dichloromethane to obtain a white solid. Yield: 13 mg (19.3%); mp: 240-245 °C; MS [M+H]⁺: 570.1; ¹H-NMR[300 MHz, DMSO-*d*₆] δ 9.58 (s, 1H, -NHCONH-), 9.14 (s, 1H, -NHCONH-), 8.77 (d, *J* = 3.5 Hz, 1H, H-quinoline), 8.55 (d, *J* = 8.8 Hz, 1H, H-quinoline), 8.37 (s, 1H, H-quinazoline), 8.18 (s, 1H, H-benzene), 7.99 (d, *J* = 8.3 Hz, 1H, H-quinoline), 7.75–7.61 (m, 5H, ArH), 7.41 (s, 1H, H-quinazoline), 4.01 (d, *J* = 3.8 Hz, 6H, -OCH₃); IR (KBr): 2835, 1677, 1614, 1564, 1500, 1266, 1121, 987, 861 cm⁻¹. HPLC purity 98.7%.

N-(4-((6,7-dimethoxyquinazolin-4-yl)oxy)naphthalen-1-yl)benzenesulfonamide, **10**.

To a solution of 4-((6,7-dimethoxyquinazolin-4-yl)oxy)naphthalen-1-amine (**4a**) (150 mg, 0.43 mmol) in dry tetrahydrofuran (10 mL) was added dropwise slowly at 0 °C trimethylamine (179 μL, 1.29 mmol) and benzenesulfonyl chloride (56 μL, 0.43 mmol) and stirred for 4 h at room temperature. The reaction mixture was adjusted with saturated sodium bicarbonate solution to pH > 7, extracted with ethyl acetate, dried with Na₂SO₄ and concentrated under reduced pressure. The residue was purified by silica gel column chromatography to give a light brown solid. Yield: 195 mg (92.8%); mp: 241-243 °C; MS [M+H]⁺: 488.1; ¹H-NMR[300 MHz, DMSO-*d*₆] δ 10.36 (s, 1H, -NHSO₂-), 8.43 (s, 1H, H-quinazoline), 8.07 (d, *J* = 7.8 Hz, 1H, H-

naphthalene), 7.74–7.72 (m, 4H, ArH), 7.64–7.38 (m, 7H, ArH), 7.21 (d, $J = 8.3$ Hz, 1H, ArH), 4.01 (s, 6H, -OCH₃); IR (KBr): 3390, 1617, 1578, 1506, 1454, 1421, 1375, 1221, 1156 cm⁻¹. HPLC purity 98.0%.

N-(4-((6,7-dimethoxyquinazolin-4-yl)oxy)naphthalen-1-yl)butane-1-sulfonamide, **11**.

To a solution of 4-((6,7-dimethoxyquinazolin-4-yl)oxy)naphthalen-1-amine (**4a**) (150 mg, 0.43 mmol) in dry pyridine (5 mL) was added 1-butanefulfonyl chloride (63 μ L, 0.48 mmol) and stirred for 1 h at room temperature. The reaction mixture was washed with 1 N hydrochloric acid, extracted with ethyl acetate, dried with Na₂SO₄ and concentrated under reduced pressure. The residue was purified by silica gel column chromatography to give a light brown solid. Yield: 24 mg (12.2%); mp: 215-218 °C; MS [M+H]⁺: 468.2; ¹H-NMR[300 MHz, DMSO-*d*₆] δ 8.46 (s, 1H, -NHSO₂-), 8.34 (d, $J = 8.6$ Hz, 1H, H-quinazoline), 7.83–7.72 (m, 2H, ArH), 7.69 (t, $J = 7.0$ Hz, 1H), 7.61–7.46 (m, 3H), 7.44 (s, 1H, H-quinazoline), 4.02 (d, $J = 1.6$ Hz, 6H, -OCH₃), 3.20 (t, $J = 7.6$ Hz, 2H, -CH₂-), 1.80–1.70 (m, 2H, -CH₂-), 1.46–1.34 (m, 2H, -CH₂-), 0.87 (t, $J = 7.3$ Hz, 3H, -CH₃); IR (KBr): 1580, 1506, 1460, 1422, 1372, 1317, 1240, 1216, 1142 cm⁻¹. HPLC purity 95.8%.

1-isopropyl-4-nitro-1H-pyrazole, **13**.

To a solution of 4-nitro-1H-pyrazole (200 mg, 1.77 mmol) in dry N,N-dimethylformamide (5 mL) was added 2-bromopropane (2.83 g, 23 mmol) and potassium carbonate (3.9 g, 28.3 mmol). The reaction mixture was heated to 50 °C and stirred for 30 min. After cooling to room temperature, the reaction mixture was taken up in ethyl acetate and water. The organic phase was washed, dried and evaporated. The residue was purified by silica gel column chromatography (ethyl acetate/petroleum ether = 1/50, v/v) to give a white solid. Yield: 252 mg (92%); mp: 64-65

1
2
3 °C; ¹H-NMR[300 MHz, DMSO-*d*₆] δ 8.93 (s, 1H, ArH), 8.26 (s, 1H, ArH), 4.59-4.56 (m, 1H, -
4 CH-), 1.45 (d, *J* = 6.7 Hz, 6H, -CH₃).

7
8 *1-isopropyl-1H-pyrazol-4-amine, 14.*

9
10 A mixture of 1-isopropyl-4-nitro-1H-pyrazole (**13**) (250 mg, 1.61 mmol), 10% palladium-carbon
11 (25 mg) and ethyl acetate (3 mL) was stirred at room temperature under hydrogen atmosphere at
12 normal pressure for 5 h. The catalyst was filtered off, and the filtrate was concentrated. The oily
13 residue **14** utilized as materials without further purification. ¹H-NMR[300 MHz, DMSO-*d*₆] δ
14 7.03 (s, 1H, ArH), 6.88 (s, 1H, ArH), 4.36–4.17 (m, 1H, -CH-), 3.81 (br, 2H, -NH₂), 1.32 (d, *J* =
15 6.7 Hz, 6H, -CH₃).

16
17
18
19
20
21
22
23 *1-(bromomethyl)-4-nitro-2-(trifluoromethyl)benzene, 16.*

24
25 To a solution of 1-methyl-4-nitro-2-trifluorotoluene (200 mg, 0.97 mmol) in 1,2-dichloroethane
26 (5 mL) was added *N*-bromosuccinimide (208.2 mg, 1.17 mmol) and azodiisobutyronitrile (16
27 mg, 0.097 mmol). The reaction mixture was heated to 90 °C and maintained for 12 h. After
28 cooling to room temperature, the reaction mixture was extracted with dichloromethane, dried
29 with Na₂SO₄ and concentrated under reduced pressure. The residue was purified by silica gel
30 column chromatography (100% petroleum ether) to give the title compound. Yield: 127 mg
31 (46.01%); MS [M+H]⁺ : 283.1.

32
33
34
35
36
37
38
39
40
41
42 *4-(4-nitro-2-(trifluoromethyl)benzyl)morpholine, 17.*

43
44 To a solution of 1-bromomethyl-4-nitro-2-trifluorotoluene (**16**) (200 mg, 0.7 mmol) and
45 morpholine (122 mg, 1.4 mmol) dissolved in dry tetrahydrofuran (8 mL) was added potassium
46 carbonate (97.3 mg, 0.7 mmol) and stirred at room temperature for 16 h. The reaction mixture
47 was concentrated and the residue was purified by silica gel column chromatography to give a
48 pale yellow solid. Yield: 194.6 mg (96%); mp: 87-88 °C; MS [M+H]⁺: 291.1; ¹H-NMR[300
49
50
51
52
53
54
55
56
57
58
59
60

MHz, DMSO- d_6] δ 8.52 (d, J = 8.6 Hz, 1H, ArH), 8.42 (s, 1H, ArH), 8.12 (d, J = 8.6 Hz, 1H, ArH), 3.74 (s, 2H, -CH₂-), 3.68–3.53 (m, 4H, -CH₂-), 2.47–2.32 (m, 4H, -CH₂-).

4-(morpholinomethyl)-3-(trifluoromethyl)aniline, 18.

A mixture of 4-(4-nitro-2-(trifluoromethyl)benzyl)morpholine (**17**) (100 mg, 0.34 mmol), 10% palladium-carbon (20 mg) and ethanol (3 mL) was stirred at room temperature under hydrogen atmosphere at normal pressure for 5 h. The catalyst was filtered off, and the filtrate was concentrated to give the title compound. Yield: 88 mg (99.4%); mp: 72-74 °C; MS [M+H]⁺: 261.1; ¹H-NMR[300 MHz, DMSO- d_6] δ 7.30 (d, J = 8.3 Hz, 1H, ArH), 6.86 (s, 1H, ArH), 6.76 (d, J = 8.3 Hz, 1H, ArH), 5.46 (s, 2H-CH₂-), 3.65–3.48 (m, 4H, -CH₂-), 2.50 (d, J = 1.6 Hz, 2H, -CH₂-), 2.31 (m, 2H, -CH₂-).

1-(4-((6,7-dimethoxyquinazolin-4-yl)oxy)naphthalen-1-yl)-3-(1-isopropyl-1H-pyrazol-4-yl)urea, 19.

To a solution of 4-((6,7-dimethoxyquinazolin-4-yl)oxy)naphthalen-1-amine (**4a**) (100 mg, 0.29 mmol) in dry dichloromethane (5 mL) was added dropwise pyridine (24 μ L) and 4-nitrophenyl chloroformate (58.5 mg, 0.29 mmol) and stirred for 30 min at room temperature. Then, 1-isopropyl-1H-pyrazol-4-amine (**14**) (36.3 mg, 0.29 mmol) and trimethylamine (32 μ L) were added and stirred for 24 h at room temperature. The reaction mixture was filtered and the filter cake was recrystallized with methanol and dichloromethane to give a light white solid. Yield: 7 mg (4.8%); mp: 178-182 °C; MS [M+H]⁺: 499.2; ¹H-NMR[300 MHz, DMSO- d_6] δ 8.80 (s, 1H, -NHCONH-), 8.74 (s, 1H, -NHCONH-), 8.44 (s, 1H, H-quinazoline), 8.17 (d, J = 8.7 Hz, 1H, H-naphthalene), 8.03 (d, J = 8.4 Hz, 1H, H-naphthalene), 7.84 (s, 1H, H-quinazoline), 7.77–7.75 (m, 2H, ArH), 7.63 (t, J = 6.75 Hz, 1H, H-naphthalene), 7.58–7.35 (m, 4H, ArH), 4.52–4.37 (m,

1
2
3 1H, -CH-), 4.03 (s, 6H, -OCH₃), 1.40 (d, *J* = 6.5 Hz, 6H, -CH₃); IR (KBr): 3414, 3280, 1636,
4
5 1504, 1375, 1232 cm⁻¹. HPLC purity 96.4%.
6

7
8 *1-(4-((6,7-dimethoxyquinazolin-4-yl)oxy)naphthalen-1-yl)-3-(5-methylisoxazol-3-yl)urea, 20.*
9

10 To a solution of triphosgene (756 mg, 2.55 mmol) in dry dichloromethane (6 mL) was added
11 dropwise slowly at 0 °C 5-methylisoxazole-3-amine (500 mg, 5.1 mmol) in dry dichloromethane
12 (4 mL) and stirred for 3 h at room temperature. The reaction mixture was filtered and
13 trimethylamine was added to the filtrate until no white smoke was liberated. Then, 4-((6,7-
14 dimethoxyquinazolin-4-yl)oxy)naphthalen-1-amine (**4a**) (200 mg, 0.58 mmol) was added and
15 stirred for 24 h at room temperature. The resulting mixture was filtered, and the filter cake was
16 washed with dichloromethane to obtain a light white solid. Yield: 21 mg (7.8%); mp: >250 °C;
17 MS [M+H]⁺: 472.2; ¹H-NMR[300 MHz, DMSO-*d*₆] δ 9.90 (s, 1H, -NHCONH-), 9.13 (s, 1H, -
18 NHCONH-), 8.45 (s, 1H, H-quinazoline), 8.17 (d, *J* = 8.4 Hz, 1H, H-naphthalene), 8.04 (d, *J* =
19 8.3 Hz, 1H, H-naphthalene), 7.86–7.73 (m, 2H, ArH), 7.73 (t, *J* = 7.59 Hz, 1H, H-naphthalene),
20 7.61–7.37 (m, 3H, ArH), 6.57 (s, 1H, H-isoxazo), 4.02 (d, *J* = 3.5 Hz, 6H, -OCH₃), 2.39 (s, 3H, -
21 CH₃); IR (KBr): 3277, 1676, 1645, 1564, 1502, 1422, 1379, 1255, 1231 cm⁻¹. HPLC purity
22 95.2%.
23
24
25

26
27
28
29
30
31
32
33
34
35
36
37
38
39
40 *1-cyclopropyl-3-(4-((6,7-dimethoxyquinazolin-4-yl)oxy)naphthalen-1-yl)urea, 21.*
41

42 To a solution of 4-((6,7-dimethoxyquinazolin-4-yl)oxy)naphthalen-1-amine (**4a**) (200 mg, 0.58
43 mmol) in dry dichloromethane (10 mL) was added dropwise pyridine (48 μL) and 4-nitrophenyl
44 chloroformate (117 mg, 0.58 mmol) and stirred for 30 min at room temperature. Then,
45 cyclopropylamine (42 μL, 0.58 mmol) and trimethylamine (48 μL) were added and stirred for 24
46 h at room temperature. The reaction mixture was filtered and the filter cake was washed with
47 dichloromethane to give a light white solid. Yield: 182.8 mg (73.1%); mp: >250 °C; MS
48
49
50
51
52
53
54
55
56
57
58
59
60

1
2
3 [M+H]⁺: 431.2; ¹H-NMR[300 MHz, DMSO-*d*₆] δ 8.49 (s, 1H, -NHCONH-), 8.43 (s, 1H, -
4 NHCONH-), 8.12 (d, *J* = 8.5 Hz, 1H, H-naphthalene), 7.98 (d, *J* = 8.4 Hz, 1H, H-naphthalene),
5 7.74–7.72 (m, 2H, ArH), 7.65 (t, *J* = 7.26 Hz, 1H, H-naphthalene), 7.54 (m, *J* = 7.26 Hz, 1H, H-
6 naphthalene), 7.45–7.35 (m, 2H, ArH), 6.8 (d, *J* = 2.7 Hz, 1H, H-naphthalene), 4.02 (d, *J* = 2.8
7 Hz, 6H, -OCH₃), 2.68–2.57 (m, 1H, -CH-), 0.75–0.62 (m, 2H, -CH₂-), 0.55–0.42 (m, 2H, -CH₂-);
8 IR (KBr): 3254, 1640, 1568, 1508, 1455, 1422, 1376, 1231 cm⁻¹. HPLC purity 97.1%.

9
10
11
12
13
14
15
16
17 *1-(4-(1-cyanocyclopentyl)phenyl)-3-(4-((6,7-dimethoxyquinazolin-4-yl)oxy)naphthalen-1-*
18
19 *yl)urea, 22.*

20
21 To a solution of triphosgene (239 mg, 0.80 mmol) in dry dichloromethane (4 mL) was added
22 dropwise slowly at 0 °C 1-(4-aminophenyl)cyclopentane-1-carbonitrile (300 mg, 1.6 mmol) in
23 dry dichloromethane (2 mL) and stirred for 3 h at room temperature. The reaction mixture was
24 filtered and trimethylamine was added to the filtrate until no white smoke was liberated. Then, 4-
25 ((6,7-dimethoxyquinazolin-4-yl)oxy)naphthalen-1-amine (**4a**) (100 mg, 0.29 mmol) was added
26 and stirred for 24 h at room temperature. The resulting mixture was filtered and the filter cake
27 was washed with tetrahydrofuran to obtain a light white solid. Yield: 42 mg (25.9%); mp: 242-
28 245 °C; MS [M+H]⁺: 582.2; ¹H-NMR[300 MHz, DMSO-*d*₆] δ 9.20 (s, 1H, -NHCONH-), 8.87 (s,
29 1H, -NHCONH-), 8.43 (s, 1H, H-quinazoline), 8.21 (d, *J* = 8.6 Hz, 1H, H-naphthalene), 8.04 (d,
30 *J* = 8.3 Hz, 1H, H-naphthalene), 7.78–7.76 (m, 2H, ArH), 7.71 (t, *J* = 8.0 Hz, 1H, H-
31 naphthalene), 7.61–7.36 (m, 7H, ArH), 4.03 (d, *J* = 3.9 Hz, 6H), 2.40–2.37 (m, 2H, -CH₂-), 2.15–
32 1.99 (m, 2H, -CH₂-), 1.90–1.88 (m, 4H, -CH₂-); IR (KBr): 3273, 1642, 1561, 1424, 1378, 1233,
33 1187, 831 cm⁻¹. HPLC purity 96.5%.

34
35
36
37
38
39
40
41
42
43
44
45
46
47
48
49
50
51 *1-(4-((6,7-dimethoxyquinazolin-4-yl)oxy)naphthalen-1-yl)-3-(4-(morpholinomethyl)-3-*
52
53 *(trifluoromethyl)phenyl)urea, 23.*

To a solution of triphosgene (1.36 g, 7.19 mmol) in dry dichloromethane (4 mL) was added dropwise slowly at 0 °C 4-(morpholinomethyl)-3-(trifluoromethyl)aniline (**18**) (300 mg, 1.2 mmol) in dry dichloromethane (2 mL) and stirred for 24 h at room temperature. The reaction mixture was filtered and trimethylamine was added to the filtrate until no white smoke was liberated. Then, 4-((6,7-dimethoxyquinazolin-4-yl)oxy)naphthalen-1-amine (**4a**) (100 mg, 0.29 mmol) was added and stirred for 24 h at room temperature. The resulting mixture was filtered and the filter cake was washed with tetrahydrofuran to obtain a light white solid. Yield: 28 mg (15.3%); mp: 234-238 °C; MS $[M+H]^+$: 634.2; 1H -NMR[300 MHz, DMSO- d_6] δ 9.46 (s, 1H, -NHCONH-), 8.95 (s, 1H, -NHCONH-), 8.45 (s, 1H, H-quinazoline), 8.20 (d, $J = 8.3$ Hz, 1H, H-naphthalene), 8.06 (s, 1H, H-quinazoline), 8.02 (dd, $J_1 = 12.7$ Hz, $J_2 = 20.9$ Hz 1H, ArH), 7.81–7.40 (m, 8H, ArH), 4.03 (m, 6H, -CH₂-), 3.58–3.56 (m, 6H, -CH₂-), 2.38 (s, 4H, -CH₂-); IR (KBr): 3339, 1645, 1503, 1380, 1318, 1233, 1116 cm^{-1} . HPLC purity 95.5%.

Biological Assay

In Vitro Kinase Assay.

Inhibition ratio determination and IC₅₀ testing at a single concentration (10 μ M) were entrusted to Reaction Biology Corporation. Cisbio's HTRF® KinEASE™ Kit was used to test the enzyme inhibitory activity. This method utilizes a unique substrate containing a single phosphorylation site recognized by a europium cryptate (Eu(K))-labeled antibody to phosphotyrosine. Based on homogeneous time-resolved fluorescence (HTRF), all KinEASE assays involve two steps: the enzymatic step and the detection step with HTRF reagents. In the kinase reaction step, 2 μ L of VEGFR-2 kinase solution, 2 μ L of biotin substrate, and 4 μ L of compound (SEB-supplemented kinase buffer) were added to each well for incubation. Then, 2 μ L of ATP was added at room temperature (18–22 °C) to initiate the reaction, which was run for 1 h. In the second step,

1
2
3 detection reagents including 5 μ L of streptavidin-XL665 (SA-XL665) in EDTA and 5 μ L
4
5 tyrosine kinase antibody-Eu(K) in EDTA were added to each well and incubated for 1 h at room
6
7 temperature. The Beckman Coulter platform HTRF detection module was used to detect the
8
9 signal. The detection reagents catch the phosphorylated substrate and the resulting HTRF signal
10
11 is proportional to the amount of phosphorylation.⁶³ According to the initial screening results,
12
13 compounds **6-8**, **10-11**, and **19-23** were diluted in 8 gradient concentrations for rescreening.
14
15 GraphPad Prism 5.0 software was used to calculate the IC₅₀ values for each compound
16
17 (<https://www.graphpad.com/scientific-software/prism/>). Each test was repeated three times.
18
19

20 21 *Anti-proliferative assay*

22 **Endothelial Cell Proliferation Assays.**

23
24 All cell activity tests were entrusted to Crown Bioscience Inc. The luciferase in the CTG reagent
25
26 uses luciferin, ATP and oxygen as substrates to produce oxidized luciferin and release energy in
27
28 the form of light. The amount of light produced is proportional to the total amount of ATP,
29
30 which can reflect the total number of viable cells (HUVECs, MDA-MB-435 and A431). The
31
32 anti-cell proliferation rate can be calculated by the fluorescence intensity. This method included
33
34 several steps. The first step is cell planking, where the cells in the exponential growth phase were
35
36 collected and the viable cells were counted with Vi-Cell XR cell counting instrument. According
37
38 to the density in the cell culture medium, the cell suspension was adjusted and 90 μ L of was
39
40 added to each well of a 96-well cell culture plate. The final cell concentration was approximately
41
42 2000 to 4000 cells per well (the specific cell density was adjusted according to cell growth). The
43
44 next step was compound dispensation, where the target compound was dissolved from 10 mM
45
46 stock solutions in DMSO, and then these solutions were diluted 10-fold with the medium
47
48 solution. A total of 10 μ L of the 10-fold compound dilution was added per well to each cell line,
49
50
51
52
53
54
55
56
57
58
59
60

1
2
3 leading to a final drug concentration of 10 μM and a final DMSO concentration of 0.1%. The
4
5 plate was placed in an incubator containing 5% CO_2 at 37°C for 72 h. Nexy was the plate
6
7 detection step, where according to the manufacturer instructions, 50 μL of CTG solution that was
8
9 previously thawed and equilibrated to room temperature was added to each well after 72 h of
10
11 drug treatment. A microplate oscillator was used to mix the solution for 2 min. After a 10-min
12
13 incubation at room temperature, the fluorescence signal value was measured by an Envision2104
14
15 plate reader. Those with the cell inhibition over than 80% at 10 μM concentration were further
16
17 submitted for a 10 concentrations test (from 1 nM to 100 μM). Data processing: inhibition
18
19 ratio= $1 - V_{\text{sample}}/V_{\text{vehicle control}} * 100\%$. V_{sample} is for drug treatment group while $V_{\text{vehicle control}}$ is for
20
21 solvent control group. The GraphPad Prism 5.0 software was used to draw nonlinear regression
22
23 model and S type dose survival rate curve, and then calculate IC_{50} values. Each test was repeated
24
25 three times.
26
27
28
29

30 31 **The growth percent on 60 cell lines by NCI**

32
33 All detailed growth methodology is described on the NCI website
34
35 (https://dtp.cancer.gov/discovery_development/nci-60/methodology.htm). Only those
36
37 compounds that exhibited significant growth inhibition in the One-Dose Screen were evaluated
38
39 against the 60 cell line panel at five concentrations. The human tumor cell lines for the cancer
40
41 screening panel were grown in RPMI 1640 medium that included 5% fetal bovine serum and 2
42
43 mM L-glutamine. Cells were inoculated into 96 well microtiter plates in 100 μL aliquots at
44
45 plating densities ranging from 5,000 to 40,000 cells/well based on the doubling time of
46
47 individual cell lines. Prior to the addition of experimental drugs, the microtiter plates were
48
49 incubated at 37 °C, 5% CO_2 , 95% air and 100% relative humidity for 24 h after cell inoculation.
50
51
52 Then, after 24 h, two plates of each cell line were fixed *in situ* with trichloroacetic acid (TCA),
53
54
55
56
57
58
59
60

1
2
3 representing a measurement of the cell population for each cell line at the time of drug addition
4 (Tz). Experimental drugs were solubilized in dimethyl sulfoxide (DMSO) at 400-fold greater
5 than the desired final maximum test concentration and stored frozen prior to use. At the time of
6 drug addition, an aliquot of frozen concentrate was thawed and diluted to twice the desired final
7 maximum test concentration with complete medium containing 50 µg/mL gentamicin.
8
9

10
11
12
13
14 After drug addition, the plates were incubated for an additional 48 h at 37 °C, 5% CO₂, 95%
15 air, and 100% relative humidity. For adherent cells, the assay was terminated by the addition of
16 cold TCA. Cells were fixed *in situ* by the gentle addition of 50 µL of cold 50% (w/v) TCA (final
17 concentration 10% TCA) and incubated for 60 min at 4 °C. The supernatant was discarded, and
18 the plates were washed five times with tap water and air dried. Sulforhodamine B (SRB) solution
19 (100 µL) at 0.4% (w/v) in 1 % acetic acid was added to each well, and the plates were incubated
20 for 10 min at room temperature. After staining, unbound dye was removed by washing five times
21 with 1% acetic acid and the plates were air dried. The bound stain was subsequently solubilized
22 with 10 mM Trizma base, and the absorbance was read by an automated plate reader at 515 nm.
23
24 For cell suspensions, the methodology was the same except that the assay was terminated by
25 fixing the settled cells at the bottom of the wells by gently adding 50 µL of 80% TCA (final
26 concentration, 16% TCA). Using seven absorbance measurements including time zero (Tz),
27 control growth (C), and test growth in the presence of drug (Ti), the percentage growth was
28 calculated at each of the drug concentrations levels. The percent growth inhibition was calculated
29 as: $[(Ti-Tz)/(C-Tz)] * 100$ for concentrations for which $Ti \geq Tz$, and $[(Ti-Tz)/Tz] * 100$ for
30 concentrations for which $Ti < Tz$.
31
32
33
34
35
36
37
38
39
40
41
42
43
44
45
46
47
48
49

50
51 Two dose response parameters were calculated for each experimental agent. Growth inhibition
52 of 50% (GI₅₀) was calculated from $[(Ti-Tz)/(C-Tz)] * 100 = 50$, which is the drug concentration
53
54
55
56
57
58
59
60

1
2
3 resulting in a 50% reduction in the net protein increase (as measured by SRB staining) in control
4 cells during drug incubation. The LC₅₀ (concentration of drug resulting in a 50% reduction in the
5 measured protein at the end of the drug treatment as compared to that at the beginning),
6 indicating a net loss of cells following treatment. It was calculated from $[(Ti-Tz)/Tz] * 100 = -50$.
7
8 Values were calculated for each of these three parameters if the desired level of activity was
9 reached; however, if the effect was not reached or was exceeded, the value for that parameter
10 was expressed as greater or less than the maximum or minimum concentration tested.
11
12
13
14
15
16
17
18
19

20 ASSOCIATED CONTENT

21 Supporting Information

22
23
24 **Figure S1.** RMSD values for the 24 crystal structures [protein (blue) and ligand (orange)] during
25 the 20 ns MD simulation. **Figure S2** Number of hydrogen bonds for the 24 crystal ligands during
26 the 20 ns MD simulation. **Figure S3** RMSD values and the number of hydrogen bonds for 9
27 designed compounds during the 20 ns MD simulation. **Figure S4** Delta G distribution of all 28
28 crystal ligands during the 20 ns simulation. **Figure S5** Delta G distribution of the 10 designed
29 compounds during the 20 ns simulation. **Figures S6-S9** Developmental therapeutics program one
30 dose mean graph of the growth percent of cell lines for compounds **6**, **19**, **22**, and **23**,
31 respectively. **Figure S10** Developmental therapeutics program five dose mean graph of the
32 growth percent as well as GI₅₀, LC₅₀ and TGI values against 58 cell lines for compound **23**.
33
34 **Figures S11–S13** Comparison of GI₅₀, TGI and LC₅₀ values, respectively, of individual the cell
35 lines for compound **23**, sorafenib and sunitinib. **Table S1** Dataset for building the binding
36 affinity model. **Table S2** Enzymatic inhibition rate of compound **23** against the targets with
37 relatively high sequence identity with VEGFR-2 from the Kinome wide screening.
38
39 Molecular_Formula_Strings.csv includes the SMILES format of the 10 designed compounds.
40
41
42
43
44
45
46
47
48
49
50
51
52
53
54
55
56
57
58
59
60

Docking_results_for_in-house_compound-database.zip is the in-house database generated by BREED and scored by molecular docking. Compound_docking_complexes.zip includes the docking complexes between VEGFR-2 (PDB: 3EWH) and the compounds.

AUTHOR INFORMATION

Corresponding Authors

For Yu Jiao: Tel.: +86-25-86185201. Fax: +86-25-86185182. E-mail: jiaoyu@cpu.edu.cn

For Tao Lu: Tel.: +86-25-86185180. Fax: +86-25-86185179. E-mail: lutao@cpu.edu.cn

Author Contributions

The manuscript was written through contributions of all authors. All authors have given approval to the final version of the manuscript. All authors contributed equally.

Conflict of interest

The authors declare no competing financial interest.

Funding Sources

The work was funded by National Natural Science Foundation of China (81302634, 21302225), the Natural Science Foundation of Jiangsu Province (BK20130662), the Fundamental Research Funds for the Central Universities (PT2014LX0072), the Priority Academic Program Development of Jiangsu Higher Education Institutions (PAPD), and the Jiangsu Qinglan Project.

ACKNOWLEDGMENTS

We would like to thank the NCI Division of Cancer Treatment & Diagnosis for the NCI-60 screening of our compounds. And we would like to thank Dr. C. Leigh Allen for revising the language of our manuscript.

ABBREVIATIONS USED

1
2
3 VEGF, vascular endothelial growth factor; VEGFR-2, vascular endothelial growth factor
4 receptor 2; TKI, tyrosine kinase inhibitors; HUVECs, human umbilical vein endothelial cells;
5
6
7 CNS cancer, central nervous system cancer; NCI, National Cancer Institute; NSCLC, non-small
8 cell lung cancer; PlGF, placental growth factor; FDA, Food and Drug Administration; CFDA,
9
10 China Food and Drug Administration; FBDD, fragment-based drug design; MM/PBSA,
11
12 Molecular Mechanics/Poisson–Boltzmann Surface Area; MD, molecular dynamics; 3D-QSAR,
13
14 three-dimensional quantitative structure activity relationship; PDB, protein data bank; PAINS,
15
16 pan assay interference compounds; RMSD, root-mean-square deviation; TGI, total growth
17
18 inhibition; HTRF, homogeneous time resolved fluorescence.
19
20
21
22
23

24 REFERENCES

- 25
26
27 (1) Holmes, K.; Roberts, O. L.; Thomas, A. M.; Cross, M. J. Vascular endothelial growth
28 factor receptor-2: structure, function, intracellular signalling and therapeutic inhibition. *Cell*
29 *Signal.* **2007**, *19*, 2003-2012.
30
31
32
33 (2) Folkman, J.; Klagsbrun, M. Angiogenic factors. *Science* **1987**, *235*, 442-447.
34
35 (3) Kiselyov, A.; Balakin, K. V.; Tkachenko, S. E. VEGF/VEGFR signalling as a target for
36 inhibiting angiogenesis. *Expert Opin. Investig. Drugs* **2007**, *16*, 83-107.
37
38 (4) Musumeci, F.; Radi, M.; Brullo, C.; Schenone, S. Vascular endothelial growth factor
39 (VEGF) receptors: drugs and new inhibitors. *J. Med. Chem.* **2012**, *55*, 10797-10822.
40
41 (5) Folkman, J. Angiogenesis in cancer, vascular, rheumatoid and other disease. *Nat. Med.*
42 **1995**, *1*, 27-30.
43
44 (6) Liotta, L. A.; Steeg, P. S.; Stetler-Stevenson, W. G. Cancer metastasis and angiogenesis:
45 an imbalance of positive and negative regulation. *Cell* **1991**, *64*, 327-336.
46
47
48
49
50
51
52
53
54
55
56
57
58
59
60

- 1
2
3 (7) Folkman, J. Anti-angiogenesis: new concept for therapy of solid tumors. *Ann. Surg.* **1972**,
4 *175*, 409-416.
5
6
7
8 (8) Bold, G.; Schnell, C.; Furet, P.; McSheehy, P.; Brügggen, J.; Mestan, J. r.; Manley, P. W.;
9 Drückes, P.; Burglin, M.; Dürler, U. A novel potent oral series of VEGFR2 inhibitors abrogate
10 tumor growth by inhibiting angiogenesis. *J. Med. Chem.* **2015**, *59*, 132-146.
11
12
13
14 (9) Plate, K. H.; Breier, G.; Weich, H. A.; Risau, W. Vascular endothelial growth factor is a
15 potential tumour angiogenesis factor in human gliomas in vivo. *Nature* **1992**, *359*, 845-848.
16
17
18
19 (10) Carmeliet, P.; Ferreira, V.; Eberhardt, C.; Declercq, C.; Pawling, J.; Moons, L.; Collen,
20 D. Development and lethality in embryos lacking a single VEGF allele. *Nature* **1996**, *380*, 435-
21 439.
22
23
24
25
26 (11) Huang, L.; Huang, Z.; Bai, Z.; Xie, R.; Sun, L.; Lin, K. Development and strategies of
27 VEGFR-2/KDR inhibitors. *Future. Med. Chem.* **2012**, *4*, 1839-1852.
28
29
30
31 (12) Boyer, S. J. Small molecule inhibitors of KDR (VEGFR-2) kinase: an overview of
32 structure activity relationships. *Curr. Top. Med. Chem.* **2002**, *2*, 973-1000.
33
34
35
36 (13) Wu, P.; Nielsen, T. E.; Clausen, M. H. FDA-approved small-molecule kinase inhibitors.
37 *Trends Pharmacol. Sci.* **2015**, *36*, 422-439.
38
39
40 (14) Zhang, Y.; Yang, S.; Jiao, Y.; Liu, H.; Yuan, H.; Lu, S.; Ran, T.; Yao, S.; Ke, Z.; Xu, J.;
41 Xiong, X.; Chen, Y.; Lu, T. An integrated virtual screening approach for VEGFR-2 inhibitors. *J.*
42 *Chem. Inf. Model* **2013**, *53*, 3163-3177.
43
44
45
46 (15) Ellis, L. M.; Hicklin, D. J. Pathways mediating resistance to vascular endothelial growth
47 factor-targeted therapy. *Clin. Cancer Res.* **2008**, *14*, 6371-6375.
48
49
50
51 (16) Jayson, G. C.; Kerbel, R.; Ellis, L. M.; Harris, A. L. Antiangiogenic therapy in oncology:
52 current status and future directions. *Lancet* **2016**, *388*, 518-529.
53
54
55
56
57
58
59
60

- 1
2
3 (17) Kuczynski, E. A.; Yin, M.; Bar-Zion, A.; Lee, C. R.; Butz, H.; Man, S.; Daley, F.;
4 Vermeulen, P. B.; Yousef, G. M.; Foster, F. S. Co-option of liver vessels and not sprouting
5 angiogenesis drives acquired sorafenib resistance in hepatocellular carcinoma. *J. Natl. Cancer*
6 *Inst.* **2016**, *108*, 1-13.
7
8
9
10
11 (18) Grothey, A. VEGF inhibition beyond tumour progression. *Lancet Oncol.* **2013**, *14*, 2-3.
12
13 (19) von Minckwitz, G.; Puglisi, F.; Cortes, J.; Vrdoljak, E.; Marschner, N.; Zielinski, C.;
14 Villanueva, C.; Romieu, G.; Lang, I.; Ciruelos, E. Bevacizumab plus chemotherapy versus
15 chemotherapy alone as second-line treatment for patients with HER2-negative locally recurrent
16 or metastatic breast cancer after first-line treatment with bevacizumab plus chemotherapy
17 (TANIA): an open-label, randomised phase 3 trial. *Lancet Oncol.* **2014**, *15*, 1269-1278.
18
19
20
21
22
23
24
25 (20) Escudier, B.; Szczylik, C.; Porta, C.; Gore, M. Treatment selection in metastatic renal cell
26 carcinoma: expert consensus. *Nat. Rev. Clin. Oncol.* **2012**, *9*, 327-337.
27
28
29
30
31 (21) Davis, M. I.; Hunt, J. P.; Herrgard, S.; Ciceri, P.; Wodicka, L. M.; Pallares, G.; Hocker,
32 M.; Treiber, D. K.; Zarrinkar, P. P. Comprehensive analysis of kinase inhibitor selectivity. *Nat.*
33 *Biotechnol.* **2011**, *29*, 1046-1051.
34
35
36
37 (22) Barouch-Bentov, R.; Sauer, K. Mechanisms of drug resistance in kinases. *Expert Opin.*
38 *Investig. Drugs* **2011**, *20*, 153-208.
39
40
41
42 (23) Pierce, A. C.; Rao, G.; Bemis, G. W. BREED: generating novel inhibitors through
43 hybridization of known ligands. application to CDK2, p38, and HIV protease. *J. Med. Chem.*
44 **2004**, *47*, 2768-2775.
45
46
47
48 (24) van Linden, O. P.; Kooistra, A. J.; Leurs, R.; de Esch, I. J.; de Graaf, C. KLIFS: a
49 knowledge-based structural database to navigate kinase–ligand interaction space. *J. Med. Chem.*
50 **2013**, *57*, 249-277.
51
52
53
54
55
56
57
58
59
60

- 1
2
3 (25) Zhang, Y.; Liu, H.; Jiao, Y.; Yuan, H.; Wang, F.; Lu, S.; Yao, S.; Ke, Z.; Tai, W.; Jiang,
4 Y. De novo design of N-(pyridin-4-ylmethyl) aniline derivatives as KDR inhibitors: 3D-QSAR,
5 molecular fragment replacement, protein-ligand interaction fingerprint, and ADMET prediction.
6 *Mol. Divers.* **2012**, *16*, 787-802.
7
8 (26) Yuan, Y.; Pei, J.; Lai, L. Binding site detection and druggability prediction of protein
9 targets for structure-based drug design. *Curr. Pharm. Design* **2013**, *19*, 2326-2333.
10
11 (27) Ngan, C. H.; Bohnuud, T.; Mottarella, S. E.; Beglov, D.; Villar, E. A.; Hall, D. R.;
12 Kozakov, D.; Vajda, S. FTMAP: extended protein mapping with user-selected probe molecules.
13 *Nucleic. Acids. Res.* **2012**, *40*, 271-275.
14
15 (28) Zhang, Y.; Zhang, D.; Tian, H.; Jiao, Y.; Shi, Z.; Ran, T.; Liu, H.; Lu, S.; Xu, A.; Qiao, X.
16 Identification of covalent binding sites targeting cysteines based on computational approaches.
17 *Mol. Pharm.* **2016**, *13*, 3106-3118.
18
19 (29) Zhang, Y.; Jiao, Y.; Xiong, X.; Liu, H.; Ran, T.; Xu, J.; Lu, S.; Xu, A.; Pan, J.; Qiao, X.
20 Fragment virtual screening based on bayesian categorization for discovering novel VEGFR-2
21 scaffolds. *Mol. Divers.* **2015**, *19*, 895-913.
22
23 (30) Kirchmair, J.; Markt, P.; Distinto, S.; Schuster, D.; Spitzer, G. M.; Liedl, K. R.; Langer,
24 T.; Wolber, G. The protein data bank (PDB), its related services and software tools as key
25 components for in silico guided drug discovery. *J. Med. Chem.* **2008**, *51*, 7021-7040.
26
27 (31) Baell, J. B.; Holloway, G. A. New substructure filters for removal of pan assay
28 interference compounds (PAINS) from screening libraries and for their exclusion in bioassays. *J.*
29 *Med. Chem.* **2010**, *53*, 2719-2740.
30
31 (32) Zhou, Q.; Chen, X.-Y.; Yang, Z.-M.; Wu, Y.-L. The changing landscape of clinical trial
32 and approval processes in China. *Nat. Rev. Clin. Oncol.* **2017**, *10*, 1-7.
33
34
35
36
37
38
39
40
41
42
43
44
45
46
47
48
49
50
51
52
53
54
55
56
57
58
59
60

- 1
2
3 (33) Park, H.-J.; Zhang, Y.; Georgescu, S. P.; Johnson, K. L.; Kong, D.; Galper, J. B. Human
4 umbilical vein endothelial cells and human dermal microvascular endothelial cells offer new
5 insights into the relationship between lipid metabolism and angiogenesis. *Stem Cell Rev. Rep.*
6 **2006**, *2*, 93-101.
7
8
9
10
11 (34) Ross, D. T.; Scherf, U.; Eisen, M. B.; Perou, C. M.; Rees, C.; Spellman, P.; Iyer, V.;
12 Jeffrey, S. S.; Van de Rijn, M.; Waltham, M. Systematic variation in gene expression patterns in
13 human cancer cell lines. *Nat. Genet.* **2000**, *24*, 227-235.
14
15
16
17
18 (35) Stanton, P.; Richards, S.; Reeves, J.; Nikolic, M.; Edington, K.; Clark, L.; Robertson, G.;
19 Souter, D.; Mitchell, R.; Hendler, F. Epidermal growth factor receptor expression by human
20 squamous cell carcinomas of the head and neck, cell lines and xenografts. *Br. J. Cancer* **1994**, *70*,
21 427-433.
22
23
24
25
26
27 (36) Wang, H.; Gao, H.; Guo, N.; Niu, G.; Ma, Y.; Kiesewetter, D.; Chen, X. Site-specific
28 labeling of scVEGF with fluorine-18 for positron emission tomography imaging. *J. Nucl. Med.*
29 **2012**, *53*, 1531-1531.
30
31
32
33
34 (37) Cerezo, A. B.; Hornedo-Ortega, R.; Álvarez-Fernández, M. A.; Troncoso, A. M.; García-
35 Parrilla, M. C. Inhibition of VEGF-Induced VEGFR-2 activation and HUVEC migration by
36 melatonin and other bioactive indolic compounds. *Nutrients* **2017**, *9*, 249.
37
38
39
40
41 (38) Xu, M.; Jin, H.; Chen, Z.; Xie, W.; Wang, Y.; Wang, Y.; Wang, M.; Zhang, J.;
42 Acheampong, D. O. A novel bispecific diabody targeting both vascular endothelial growth factor
43 receptor 2 and epidermal growth factor receptor for enhanced antitumor activity. *Biotechnol.*
44 *Progr.* **2016**, *32*, 294-302.
45
46
47
48
49 (39) Chow, L. Q.; Eckhardt, S. G. Sunitinib: from rational design to clinical efficacy. *J. Clin.*
50 *Oncol.* **2007**, *25*, 884-896.
51
52
53
54
55
56
57
58
59
60

- 1
2
3 (40) Norris-Cervetto, E.; Callaghan, R.; Platt, F. M.; Dwek, R. A.; Butters, T. D. Inhibition of
4 glucosylceramide synthase does not reverse drug resistance in cancer cells. *J. Biol. Chem.* **2004**,
5
6 279, 40412-40418.
7
8
9
10 (41) Padro, T.; Bieker, R.; Ruiz, S.; Steins, M.; Retzlaff, S.; Bürger, H.; Büchner, T.; Kessler,
11
12 T.; Herrera, F.; Kienast, J. Overexpression of vascular endothelial growth factor (VEGF) and its
13
14 cellular receptor KDR (VEGFR-2) in the bone marrow of patients with acute myeloid leukemia.
15
16 *Leukemia* **2002**, 16, 1302-1310.
17
18
19 (42) Stefanik, D.; Harmey, J. H. Vascular Endothelial Growth Factor in Malignant Disease of
20
21 the Central Nervous System. *VEGF and Cancer* **2011**, 72-82.
22
23
24 (43) Dias, S.; Hattori, K.; Zhu, Z.; Heissig, B.; Choy, M.; Lane, W.; Wu, Y.; Chadburn, A.;
25
26 Hyjek, E.; Gill, M. Autocrine stimulation of VEGFR-2 activates human leukemic cell growth
27
28 and migration. *J. Clin. Invest.* **2000**, 106, 511-521.
29
30
31 (44) Salven, P.; Heikkila, P.; Joensuu, H. Enhanced expression of vascular endothelial growth
32
33 factor in metastatic melanoma. *Br. J. Cancer* **1997**, 76, 930-934.
34
35
36 (45) Mehnert, J. M.; McCarthy, M. M.; Jilaveanu, L.; Flaherty, K. T.; Aziz, S.; Camp, R. L.;
37
38 Rimm, D. L.; Kluger, H. M. Quantitative expression of VEGF, VEGF-R1, VEGF-R2, and
39
40 VEGF-R3 in melanoma tissue microarrays. *Hum. Pathol.* **2010**, 41, 375-384.
41
42
43 (46) Molhoek, K. R.; Griesemann, H.; Shu, J.; Gershenwald, J. E.; Brautigan, D. L.; Slingluff,
44
45 C. L. Human melanoma cytotoxicity by combined inhibition of mammalian target of rapamycin and
46
47 vascular endothelial growth factor/vascular endothelial growth factor receptor-2. *Cancer Res.*
48
49 **2008**, 68, 4392-4397.
50
51
52
53
54
55
56
57
58
59
60

- 1
2
3 (47) Molhoek, K. R.; Erdag, G.; Rasamny, J.; Murphy, C.; Deacon, D.; Patterson, J. W.;
4 Slingluff, C. L.; Brautigan, D. L. VEGFR-2 expression in human melanoma: Revised assessment.
5
6 *Int. J. Cancer* **2011**, *129*, 2807-2815.
7
8
9
10 (48) Pla, A. F.; Brossa, A.; Bernardini, M.; Genova, T.; Grolez, G.; Villers, A.; Leroy, X.;
11 Prevarskaya, N.; Gkika, D.; Bussolati, B. Differential sensitivity of prostate tumor derived
12 endothelial cells to sorafenib and sunitinib. *BMC Cancer* **2014**, *14*, 939-951.
13
14
15
16 (49) Chartier, M.; Chenard, T.; Barker, J.; Najmanovich, R. Kinome render: a stand-alone and
17 web-accessible tool to annotate the human protein kinome tree. *PeerJ* **2013**, *1*, 1-16.
18
19
20 (50) Li, Y. H.; Wang, P. P.; Li, X. X.; Yu, C. Y.; Yang, H.; Zhou, J.; Xue, W. W.; Tan, J.; Zhu,
21 F. The human kinome targeted by FDA approved multi-target drugs and combination products: a
22 comparative study from the drug-target interaction network perspective. *PloS One* **2016**, *11*,
23 e0165737.
24
25
26 (51) Cohen, P. Protein kinases--the major drug targets of the twenty-first century? *Nat. Rev.*
27 *Drug Discov.* **2002**, *1*, 309-315.
28
29
30
31 (52) Morphy, R. Selectively nonselective kinase inhibition: striking the right balance. *J. Med.*
32 *Chem.* **2009**, *53*, 1413-1437.
33
34
35 (53) Broekman, F.; Giovannetti, E.; Peters, G. J. Tyrosine kinase inhibitors: Multi-targeted or
36 single-targeted? *World J. Clin. Oncol.* **2011**, *2*, 80-93.
37
38
39 (54) Schrodinger, L. Schrodinger software suite. *New York: Schrödinger, LLC* **2011**.
40
41
42 (55) Halgren, T. New Method for Fast and Accurate Binding-site Identification and Analysis.
43 *Chem. Biol. Drug. Des.* **2007**, *69*, 146-148.
44
45
46 (56) Van Der Spoel, D.; Lindahl, E.; Hess, B.; Groenhof, G.; Mark, A. E.; Berendsen, H. J.
47 GROMACS: fast, flexible, and free. *J. Comput. Chem.* **2005**, *26*, 1701-1718.
48
49
50
51
52
53
54
55
56
57
58
59
60

- 1
2
3 (57) Duan, Y. W., C.; Chowdhury, S.; Lee, M. C.; Xiong, G.; Zhang, W.; Yang, R. C., P.;
4 Luo, R.; Lee, T.; Caldwell, J.; Wang, J.; Kollman, P. A point-charge force field for molecular
5 mechanics simulations of proteins based on condensed-phase quantum mechanical calculations. *J.*
6 *Comput. Chem.* **2003**, *24*, 1999-2012.
7
8 (58) Jorgensen, W. L. Quantum and statistical mechanical studies of liquids. 10. Transferable
9 intermolecular potential functions for water, alcohols, and ethers. Application to liquid water. *J.*
10 *Am. Chem. Soc.* **1981**, *103*, 335-340.
11
12 (59) Hess, B. P-LINCS: A parallel linear constraint solver for molecular simulation. *J. Chem.*
13 *Theory Comput.* **2008**, *4*, 116-122.
14
15 (60) Miller, B. R.; McGee, T. D.; Swails, J. M.; Homeyer, N.; Gohlke, H.; Roitberg, A. E.
16 MMPBSA.py: an efficient program for end-state free energy calculations. *J. Chem. Theory*
17 *Comput.* **2012**, *8*, 3314-3321.
18
19 (61) Chéron, N.; Jasty, N.; Shakhnovich, E. I. OpenGrowth: an automated and rational
20 algorithm for finding new protein ligands. *J. Med. Chem.* **2016**, *59*, 4171-4188.
21
22 (62) Swetha, R. G.; Ramaiah, S.; Anbarasu, A. Molecular dynamics studies on D835N
23 mutation in FLT3-its impact on FLT3 protein structure. *J. Cell. Biochem.* **2016**, *117*, 1439-1445.
24
25 (63) Tardieu, J.-L. HTRF® KinEASE™ TK: a new solution for tyrosine kinase screening. *Nat.*
26 *Methods* **2007**, *4*, i-ii.
27
28
29
30
31
32
33
34
35
36
37
38
39
40
41
42
43
44
45
46
47
48
49
50
51
52
53
54
55
56
57
58
59
60

TABLE OF CONTENTS GRAPHIC

